Experimental optimization of second-order harmonic generation for higher-order generation applications

by Julia Strömberg

LUNDS UNIVERSITET

B.Sc. Thesis
Supervisor: David Busto
Assistant Supervisor: Edoardo Alberto Boati
Examiner: Jörgen Larsson

LRAP: 604
Division of Atomic Physics
Department of Physics
Lund University, Faculty of Engineering (LTH)
Lund, Sweden
September 2024

Abstract

An atom interacting with a strong laser field can give rise to high-order harmonic generation (HHG), a non-perturbative, highly non-linear process. The resulting HHG spectrum is a comb of odd harmonics. For some experiments, a large energy difference between consecutive harmonics is beneficial. In order to achieve a larger spacing between harmonics, second-harmonic (SH) radiation resulting from another type of non-linear process can be used to drive HHG. Second-harmonic generation (SHG) is, in contrast to HHG, described by perturbative treatment in the field of non-linear optics. This thesis focuses on a laser's second-order harmonic generation (SHG) with the long-term aim of using it to drive HHG. Phase-matching plays an essential role in optimizing second-harmonic conversion efficiency and sets a condition for optimal efficiency. A way to achieve this condition is by carefully controlling the angle orientation of a birefringent non-linear crystal, giving rise to SHG of different wavelengths from the input laser field.

Att utnyttja en överton för att driva högre övertoner

När atomer och molekyler interagerar med laserfält av hög intensitet kan fascinerande och oväntade fenomen uppstå. Två viktiga genombrott inom laserforskningen inträffade på 1960- respektive 1980-talet, när två besläktade men distinkta processer upptäcktes. Den senare av dessa ledde till Nobelpriset i fysik 2023, vilket skapade svensk historia.

När en högintensiv laserstråle fokuseras på en kristall med specifika egenskaper kan en bråkdel av ljuset omvandlas till ljus med dubbelt så hög frekvens som den ursprungliga strålens. Denna process kallas second-harmonic generation (SHG), där den omvandlade ljusvågen är en så kallad andra ordningens överton av det ursprungliga ljuset, vilket innebär att den nya ljusvågen har en frekvens som är två gånger det infallande laserfältets frekvens. Om intensiteten på laserstrålen ökas ytterligare och nu riktas mot en gas av atomer kan höga övertoner skapas, som når vågländer i den extrema ultravioletta regionen. I tidsdomänen motsvarar denna kam av höga övertoner ett tåg av attosekundpulser (1 as = 10^{-18} s) som kan användas för att studera elektronrörelser i materia.

Om infrarött ljus används för att driva processen för övertonsgenereringen, kommer de genererade övertonernas energier ligga nära varandra, vilket kan skapa problem för vissa attosekundexperiment. I detta fall skulle det vara fördelaktigt att generera övertoner med den andra övertonen av det fundamentala IR-fältet, vilket skapar en övertonskam med större energiseparation mellan kamtänderna. Denna rapport undersöker möjligheten att använda frekvensdubbling för att öka frekvensseparationen mellan övertonerna.

För att uppnå detta mål undersöker vi experimentellt och via numeriska simuleringar hur egenskaperna hos den andra övertonens strålning kan optimeras och justeras. Vi avslutar med att uppskatta möjligheterna att generera höga övertoner med hjälp av de genererade ljuspulserna från den andra övertonen.

Acknowledgements

I would first like to thank my supervisors, David and Edoardo. Thank you, David, for offering me the opportunity to do this project and for guiding me throughout the project. You were always patient and took the time to answer questions, discuss, and explain things in a very pedagogical way. You also taught me a completely new way of writing a scientific report, for which I am very grateful. Thank you for your invaluable feedback and truly inspirational advice. Thank you, Edoardo, for all the fun times spent in the lab and for always bringing new perspectives to my project. You always took the time to discuss things and answer questions. You always went through things methodically in the lab and were very patient when I learned the setup. I am very grateful for all your inspiring advice and for explaining things with humor. Also, thank you for broadening my knowledge of Italian culture.

Thank you, Mattias, for our insightful discussions, for teaching me Matlab hacks, for creating a positive atmosphere, and for reviewing my project. You were always enthusiastic about answering questions and giving me feedback on my ideas. Your in-depth explanations and tour of the Attolab, where you explained every detail down to a micro-level, were much appreciated.

Thank you, Anne-Lise and Christoph, for our discussions and your advice, which provided further insight and inspiration. I also want to thank Saga for helping me with LaTex, bringing a positive spirit, and letting me borrow the D-lab spectrometer. Thanks, Hugo, for giving me a crash course on FFT, being open to discussions, helping me with LaTex, and sharing the office. Your calmness and down-to-earth spirit always created a sense of mindfulness in the office.

I also would like to thank Per for being an excellent teacher and for helping me find a supervisor for the project. Also, thank you, Anne, for being such an inspiring and passionate teacher.

Finally, I would like to thank the entire Atto group and the rest of the division for creating a positive atmosphere and making me feel included and welcomed. This project has been a wonderful experience, where I had the pleasure of meeting and talking with great people. Your research and just being in your surroundings have truly inspired me in my studies. Thank you all for showing me the incredible work behind the doors.

Contents

Chapter 1

Introduction

With the development of lasers, it has become possible to reach light intensities high enough to observe optical non-linear processes in matter [1]. A typical example of non-linear light-matter interaction is SHG. SHG can easily be demonstrated by sending an ultra-short laser beam into a crystal of desired properties [1], which converts a portion of the light into secondary radiation at twice the initial frequency, called second-harmonic (SH) radiation.

The area of non-linear optics studies the interaction of light with matter in the non-linear regime, where the response of the medium to an externally applied electromagnetic field is non-linear in the amplitude of this field. The linear regime dominates at low intensities, typical of non-laser sources, where the medium properties are independent of the illumination intensity, and light waves can pass through the medium without interacting with each other. In the non-linear regime, however, the material response is a non-linear function in the amplitude of the applied electric field strength, which, in turn, can modify the behavior of the driving field [2]. The non-linear behavior is observed at high-intensity sources such as lasers. The interaction can generate optical fields at new frequencies that differ from the incident fundamental frequency. In this regime, SHG can occur, which is explained by a perturbative treatment of the light-matter interaction. For laser fields at even higher intensities, HHG can occur, which, unlike low-order harmonics, is described as a non-perturbative regime of light-matter interaction. [2]

At the end of the 1980s, HHG was discovered by focusing very intense laser pulses of time durations of the order of picoseconds [3], [4]. In the HHG spectrum, consisting of a comb of odd harmonics, it was revealed that the intensity of the higher harmonics did not continue to decrease as the order of the harmonics increased, as the perturbative model suggested, but stayed constant up to very high orders before eventually decreasing again [5]. This discovery opened the opportunity to generate attosecond pulses for the study of electron dynamics in matter, and it was awarded the Nobel Prize in 2023.

In particular, Lund University uses HHG for a wide range of applications, and the Attosecond group uses this technique to study photoionization and measure the quantum properties of photoelectrons [6]. HHG is often driven with infrared (IR) laser pulses with a central wavelength of around 800 nm. As a result, consecutive harmonics are spaced by approximately 3.1 eV. For some applications, producing higher harmonics with a greater spacing is desirable. This can be achieved by frequency doubling the IR laser using SHG, which allows an increase in the energy separation.

HHG requires high intensities at the focus. For this reason, it is essential to optimize the conversion efficiency of the SH. A common way to optimize the efficiency is to adjust the angle between the crystal used for SHG and the incoming beam such that it minimizes the phase mismatch between the IR radiation and its SH.

1.1 Scope of the work

This thesis aims to serve as a step toward implementing SHG for HHG. Thus, it intends to investigate and experimentally optimize the efficiency of SHG for HHG purposes. Two Beta Barium Borate (BBO) crystals of lengths $L = 2$ mm and $L = 200$ µm are used in a setup tailored to optimize the conversion efficiency of SH waves by angle-tuning phase matching. The setup is implemented in the Attolab in the Atomic Physics Division of Lund University, and the experimental results are compared with numerical simulations.

1.2 Thesis outline

Six chapters constitute this thesis. Chapter 1 contains a motivation for the project and a brief introduction to SHG, providing a context to the thesis. The methodology is presented along with the objectives of the project. Chapter 2 gives the necessary theoretical background for understanding, generating numerical simulations, and performing the experiments. Chapter 3 presents the experimental setup and methodology for obtaining the SHG spectra. Chapter 4 presents numerical simulations of the SHG spectra and conversion efficiency graphs. In Chapter 5, the experimental results are analyzed and compared with the simulations. Finally, in Chapter 6, a summary and conclusions of the thesis are provided. The possible improvements and applications for future research are discussed in the outlook.

Chapter 2

Background

2.1 Nonlinear optics

In linear optics, the frequency of a light beam is preserved after passing through matter. In contrast, in the nonlinear optics regime, multiple physical processes arising from the interaction of light with matter affect the electromagnetic field, leading to a frequency conversion of a fraction of the incident beam, which results in outgoing waves of frequency differing from the initial. Such effects occur at high intensities.

The non-linear response in a dielectric medium is characterized by a non-linear relationship between the polarization density, $\tilde{P}(t)$, and the external electric field $\tilde{E}(t)$. Generally, the polarization can be written in terms of a Taylor series expansion in the electric field strength [7]:

$$\tilde{P}(t) = \epsilon_0(\underbrace{\chi^{(1)}\tilde{E}(t)}_{\text{Linear}} + \underbrace{\chi^{(2)}\tilde{E}^2 + \chi^{(3)}\tilde{E}^3 + ...}_{\text{Nonlinear}}), \tag{2.1}$$

where $\tilde{P}(t)$ and $\tilde{E}(t)$ are scalar quantities and ϵ_0 is the permittivity of free space. The quantities $\chi^{(2)}$ and $\chi^{(3)}$ are the second- and third-order nonlinear optical susceptibilities, respectively. In the linear regime, which occurs for weak field strengths, Eq. (2.1) reduces to a linear relationship between $\tilde{P}(t)$ and $\tilde{E}(t)$ where $\chi^{(1)}$ is known as the linear susceptibility and is the constant of proportionality [8]. For an electric field of sufficient strength, higher-order terms start to affect the polarization density. The terms χ^n are the nth-order non-linear susceptibilities. The susceptibilities of even order, and in particular $\chi^{(2)}$, are only present in materials without inversion symmetry, such as anisotropic crystals [9].

2.1.1 Second-order harmonic generation

SHG occurs when radiation passes through a non-linear crystal, leading to the emission of secondary radiation with twice the frequency of the incident beam; see Fig. 2.1(a). In this process, two photons of identical energies combine to generate a photon with an energy equal to the sum of the initial photon energies [10]. Figure 2.1(b) schematically presents the second-harmonic generation process in which direct two-photon absorption prompts the electron to a virtual state (shown in dashed lines). The co-occurring deexcitation of the electron back to the ground state leads to the emission of a photon with twice the energy of the incident photons: $\hbar\omega_1 + \hbar\omega_1 = \hbar\omega_2$ [11].

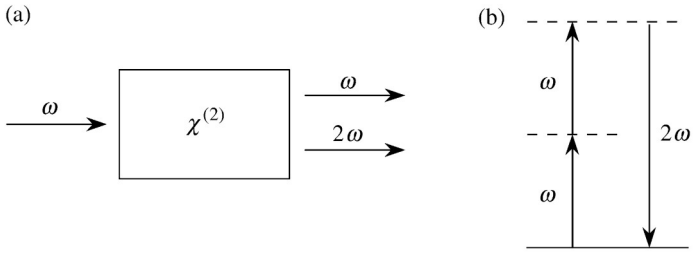

Figure 2.1: (a) A fundamental wave of angular frequency ω incident on an anisotropic crystal of non-linear susceptibility $\chi^{(2)} \neq 0$ undergoing SHG. (b) Scheme of the three-body interaction of the SHG process. Figure from [9]

.

The above description is at the microscopic level. However, when an intense light beam interacts with a macroscopic crystal, the total non-linear response results from the interference of many emitters. In order to optimize the generation of the second harmonic radiation it is essential to ensure that the different emitters radiate in phase, resulting in constructive interference. [12].

2.2 Macroscopic effects in second-order harmonic generation

The macroscopic aspects of the SHG process must be considered to understand the experimental observations of the SHG spectra. These effects include the propagation of the fundamental beam in a non-linear media, described by Maxwell's classical equations, and the collective response of atoms emitting harmonic radiation at various phases, called phase matching, a key element in optimizing conversion efficiency. [7]

2.3 Coupled-wave equations and second-harmonic conversion efficiency

The microscopic fields of radiation are described by classical electromagnetism through Maxwell's equations [10]:

$$\nabla \times \tilde{\mathbf{E}} = -\frac{\partial \tilde{\mathbf{B}}}{\partial t} \text{ (Faraday's law)} \tag{2.2}$$

$$\nabla \times \tilde{\mathbf{H}} = \frac{\partial (\tilde{\mathbf{D}})}{\partial t} + \tilde{\mathbf{J}} \text{ (Ampère's law)} \tag{2.3}$$

$$\nabla \cdot \tilde{\mathbf{D}} = \tilde{\rho} \text{ (Coulomb's law)} \tag{2.4}$$

$$\nabla \cdot \tilde{\mathbf{B}} = 0 \text{ (Absence of free magnetic poles)}, \tag{2.5}$$

where $\tilde{\rho}$ and $\tilde{\mathbf{J}}$ are the charge and current density respectively. The solution of interest concerns classical light waves given by the electric and magnetic fields ($\tilde{\mathbf{E}}$ and $\tilde{\mathbf{B}}$, respectively) for neutral dielectric media. Such media are non-conductive and non-magnetic, meaning $\tilde{\rho} = 0$ (absence of free charges), $\tilde{\rho} = 0$ (absence of currents), and $\mu = \mu_0$, which is the vacuum permeability. The induced polarization density can be divided into linear and nonlinear parts, $\tilde{\mathbf{P}} = \tilde{\mathbf{P}}^{\mathrm{L}} + \tilde{\mathbf{P}}^{\mathrm{NL}}$, and following the derivation in [9], the wave equation is given by:

$$\nabla^2 \tilde{\mathbf{E}} - \frac{\epsilon^{(1)}}{c_0^2} \frac{\partial^2 \tilde{\mathbf{E}}}{\partial t^2} = \frac{1}{\epsilon_0 c_0^2} \frac{\partial^2 \tilde{\mathbf{P}}^{\mathrm{NL}}}{\partial t^2};\ c_0 = \frac{1}{\sqrt{\mu_0 \epsilon_0}}, \tag{2.6}$$

where $\epsilon^{(1)}$ is a real, frequency-dependent dielectric tensor while ϵ_0 and c_0 are the vacuum permittivity and the speed of light in vacuum, respectively. Equation (2.6) is called the driven or inhomogeneous wave equation and describes how the non-linear interaction couples the various frequency components

of the laser field [11]. The source term on the right-hand side of the equation represents the non-linear response of the material, acting as the driving source that induces an electromagnetic wave of the same frequency as the non-linear polarization wave $\tilde{\mathbf{P}}^{\mathrm{NL}}$ [2].

Consider the scalar case of an electric field, which is a superposition of two monochromatic plane waves of frequencies ω_1 and $\omega_2 = 2\omega_1$ of slowly varying amplitudes $A_1(z)$ and $A_2(z)$, propagating in the z-direction in a dispersive and lossless (i.e., no power loss of the laser beam during transmission) non-linear crystal. The electric field strength is given by [8], [11]:

$$E(z,t) = \sum_{j}^{2} \mathrm{Re}\{A_j(z)e^{i(\omega_j t - k_j z)}\} = \sum_{j=\pm1,\pm2} \frac{1}{2} A_j e^{i(\omega_j t - k_j z)}, \tag{2.7}$$

where $\omega_{-j} = -\omega_j$, $A_{-j} = A_j^*$, and

$$k_j = \frac{n_j \omega_j}{c_0};\ n_j = [\epsilon^{(1)}(\omega_j)]^{1/2}, \tag{2.8}$$

where, k_j and n_j are the wave vector and the refractive index of the j:th component [9]. Following the derivation in the Appendix, interactions between the monochromatic waves can be described by a system of coupled equations [8]:

$$\begin{cases} \frac{dA_1}{dz} = \frac{2i\omega_1^2 d_{\mathrm{eff}}^1}{k_1 c^2} A_2 A_1^* e^{-i\Delta k z} \\ \frac{dA_2}{dz} = \frac{i\omega_2^2 d_{\mathrm{eff}}}{k_2 c^2} A_1^2 e^{i\Delta k z} \end{cases}, \tag{2.9}$$

where

$$\Delta k = 2k_1 - k_2, \tag{2.10}$$

where Δk is the so-called wave vector mismatch factor [9].

The solution to Eq. (2.9) is given by:

$$A_2(L) = i\left(\frac{4\omega_1^2}{k_2 c^2}\right) d_{\mathrm{eff}} A_1^2 \frac{e^{i\Delta k L} - 1}{i\Delta k}, \tag{2.11}$$

where L is the crystal length. Finally, the intensity of the emitted SH radiation is:

$$I_2(L) = \frac{32\pi^2}{n_2 n_1^2 \lambda_1^2 \epsilon_0 c^3} d_{\mathrm{eff}}^2 I_1^2 L^2 \,\mathrm{sinc}^2\left(\frac{\Delta k L}{2}\right). \tag{2.12}$$

For the complete derivation, see Appendix. Moreover, the SHG efficiency is defined as:

$$\eta_{\mathrm{SHG}} \coloneqq \frac{I_2(L)}{I_1(0)}, \tag{2.13}$$

which is the ratio between the SH intensity at the end of the medium and the fundamental intensity at the entrance of the medium.

Equation 2.12 also shows that in addition to propagation length L, the intensity of SH also depends on the wave-vector mismatch Δk. At the beginning of the medium ($L = 0$), the intensity of the second harmonic is zero. As the fundamental pulse propagates in the medium, the SH intensity increases. The speed with which the second harmonic signal increases with length depends on the wave vector mismatch Δk through the factor $\mathrm{sinc}^2(\frac{\Delta k}{L})$, which will be discussed in the following. Figure 2.2b) schematically presents the spectrum of light at the end of the generation medium and shows that part of the fundamental IR intensity is converted to the second harmonic.

The solution (2.12) clearly demonstrates the importance of minimizing the wave-vector mismatch Δk for efficient SHG. The SH radiation is emitted randomly from the electrons in the material,

[1] This is known as the effective d-value, see Appendix for more information.

which undermines the SH radiation because of destructive interference. To improve SHG, the radiation from all emitters must be phase-matched, which means that $\Delta k = 0$. [13] This case is illustrated in wave vectors in Fig. 2.2(c), corresponding to the conservation of momentum ($\hbar\mathbf{k}_1 + \hbar\mathbf{k}_1 = 2\hbar\mathbf{k}_1$) in the photon interaction process illustrated in Fig. 2.1. However, in general, the wave vector mismath Δk is non-zero. This is illustrated in terms of wave vectors in Fig. 2.2(d), which highlights the meaning of a non-zero wave vector mismatch.

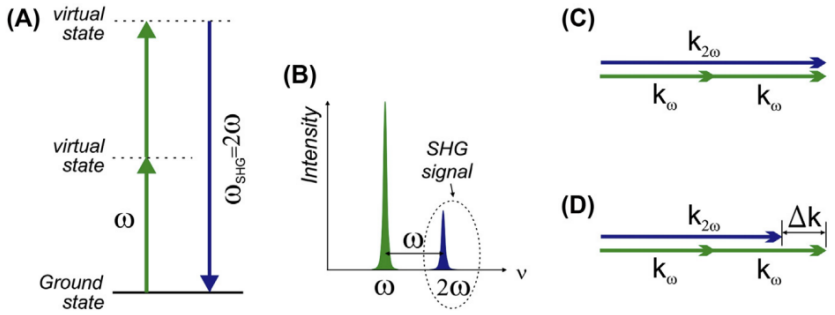

Figure 2.2: The SHG process for collinear beams: (a) energy level diagram, (b) spectral positions of input and output fields, (c) perfect collinear phase matching, and (d) wave-vector mismatch. Figure taken from [14].

The period of Eq. (2.13) is referred to as the coherence length of the non-linear interaction, $L_c = \frac{2}{|\Delta k|}$ [9]. This means that the oscillation in Eq. (2.12) can be described by $\text{sinc}^2 \frac{L}{L_c}$. The coherence length defines the length of the non-linear medium at which the SHG efficiency is maximized [11]. When $\Delta k \neq 0$, the coherence length can be interpreted as a strip of SH dipoles, each with a width of L_c, radiating constructively reinforced SH fields. When L increases beyond L_c, the SH wave can go out of phase with its driving field. Consequently, power can flow from the SH wave back into the fundamental waves; see Eq. (2.9) [9]. The combined constructive and destructive interference effects lead to the oscillatory behavior in the case of a non-zero wave vector mismatch seen in Fig. 2.3 [15]. However, when $\Delta k = 0$, Eq. (2.12) predicts a quadratic scaling growth of $I_2(L)$ as a function of L (see Fig. 2.3). In this case, the solution is said to be phase-matched, and $\Delta k = 0$ defines the so-called phase-matching condition [8]. Figure 2.3 demonstrates that a non-zero wave vector mismatch adversely affects the conversion efficiency.

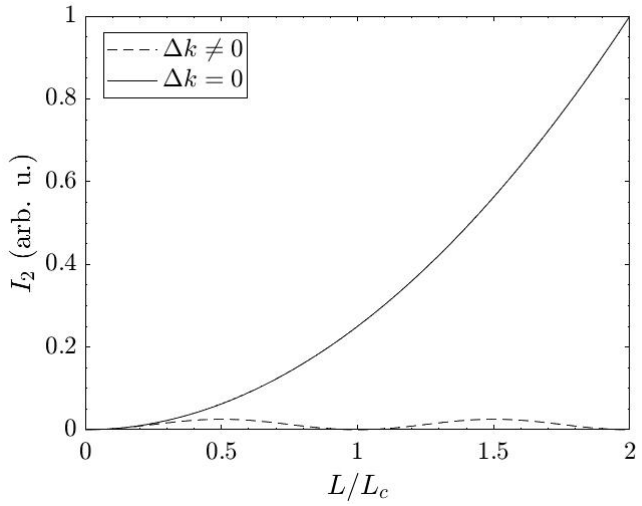

Figure 2.3: Graphical illustration of the effect of wave vector mismatch (Δk) on I_2 (normalized) of L/L_c based on a flat spectrum. In particular, $\Delta k = 0.5$.

At this point, it is important to emphasize that the beam used in the experiments is Gaussian, with an intensity profile in the transverse plane described by a spatially dependent amplitude, which needs to be accounted for in Eq. (2.6). However, the Gaussian beam is collimated in the experiments, which means that the paraxial approximation can be invoked, resulting in the same expression as in Eq. 2.12. [9]

So far, incoming radiation has been considered monochromatic. However, short light pulses composed of many frequencies are used in the experiments. The pulse duration, $\Delta\tau$ is related to the spectral bandwidth, $\Delta\nu$, according to the time-bandwidth product,

$$\Delta\tau\Delta\nu \geq \gamma, \tag{2.14}$$

where $\gamma = 0.44$ for Gaussian pulses. For equality, the pulse must be Fourier transform-limited, in other words, unchirped [11].

2.3.1 Birefringent critical phase matching in an anisotropic crystal

approximated to be a gaussian., Beam profile on page 13. From Eqs. (2.10) and (2.8) imply that in order to achieve perfect phase matching, the refractive indices of the fundamental and SH must be the same, i.e.,

$$n(\omega) = n(2\omega). \tag{2.15}$$

However, due to dispersion, the refractive index for different wavelengths is usually different, making it very difficult to fulfill this condition [9].

A solution to this problem is to use birefringent crystals, which are anisotropic materials that exhibit different refractive indices depending on the orientation of the light polarization [11]. An example of a birefringent crystal is the uniaxial crystal, characterized by a single optic axis that defines the direction in which light experiences the same refractive index despite the polarization mode [11]. In other directions, the uniaxial crystal can support two orthogonal eigenpolarization modes, an effect called birefringence [16]. Incident light is separated into two beams of distinct propagation directions, each of which experiences different refractive indices. The two distinct polarizations are known as ordinary polarization and extraordinary polarization and are associated with the ordinary and extraordinary refractive index, respectively [16].

As seen in Fig. 2.4 a), the ordinary refractive index for the fundamental wavelength λ_1 of light incident on the crystal can be represented by a circle (blue) of radius $n_o(\lambda_1)$ in the plane containing the optic axis and the propagation direction $\bar{k}$ for a negative uniaxial crystal. Such crystals are characterized by $n_e \leq n_o$ [8]. In contrast, the extraordinary refractive index n_e follows an ellipse (dashed blue curve). For SH light generated at wavelength $\lambda_2 = \lambda_1/2$, the sizes of the circle and ellipse are increased (shown in red) due to the wavelength dependence of the refractive indices [17]. It can be further seen that for both wavelengths, the ordinary and extraordinary refractive indices are equal along the optic axis.

For a transparent medium, the ordinary refractive index (n_o) and the extraordinary refractive index ($\bar{n}_e$) of the fundamental wave can be calculated from Sellmeier's equations [18]:

$$\bar{n}_e(\lambda), n_o(\lambda) = \sqrt{A + \frac{B}{\lambda^2 - C} - D\lambda^2}, \tag{2.16}$$

where λ is the wavelength. The constant coefficients A, B, C, and are empirical and medium-specific [17]. Hence, The angle dependence of the extraordinary refractive index that the SH wave experiences can be conveniently described by the following ellipse equation, as Fig. 2.4a) suggests [8]:

$$\frac{1}{n_e(\lambda_2, \theta)^2} = \frac{\sin^2\theta}{\bar{n}_e(\lambda_2)^2} + \frac{\cos^2\theta}{n_o(\lambda_2)^2}, \tag{2.17}$$

where $n_o(\lambda_2)$ and $\bar{n}_e$ are given by Eq. 2.16. In particular, $\bar{n}_e$ is the value of the extraordinary refractive index intersecting the horizontal axis in Fig. 2.4.

When using a negative uniaxial crystal to achieve phase matching for the SHG, the SH wave must be polarized so that it experiences the lowest refractive index. This choice corresponds to an extraordinary polarization [9]. For the fundamental waves, there are two choices regarding the polarization, each corresponding to a specific type of phase matching. Type I phase matching occurs when the two fundamental waves have the same polarization. In type II, their polarizations are orthogonal. In this project, the BBO crystals used are cut to support type I phase matching, i.e., the fundamental is polarized along the ordinary axis, and the SH is polarized along the extraordinary axis, as described by $n_e(\lambda_2)\omega_2 = n_o(\lambda_1)\omega_1 + n_o(\lambda_1)\omega_1$.

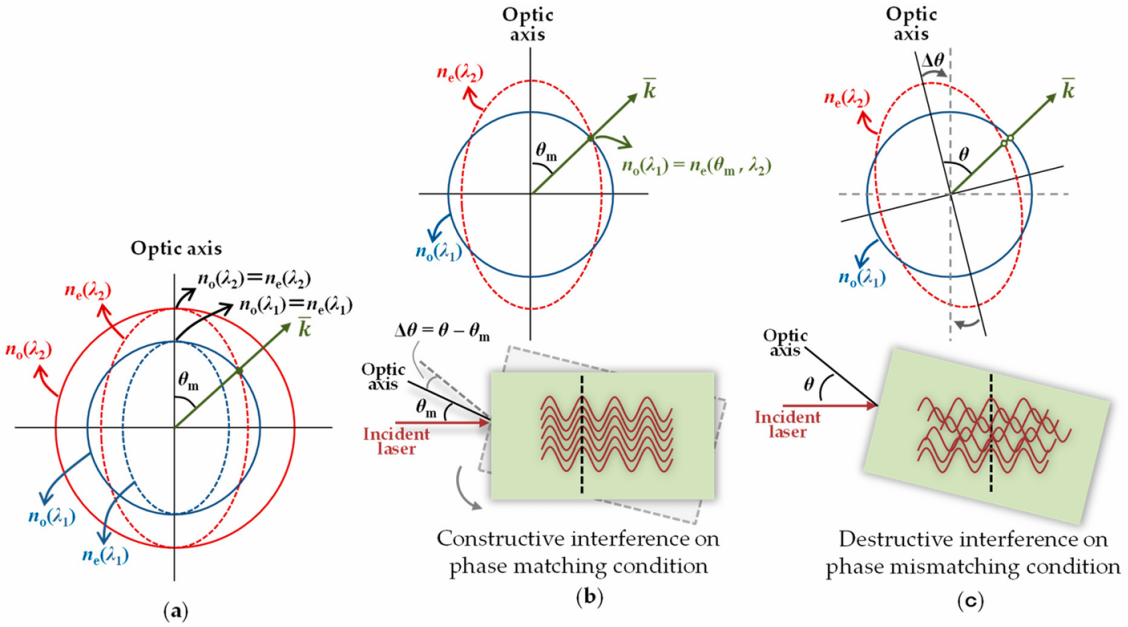

Figure 2.4: Phase matching angle θ_m for type I SHG in a negative uniaxial crystal. (a) Two-dimensional representation of refractive indices. The refractive indices experienced by the fundamental wave are shown in blue, and those experienced by the SH wave are shown in red. (b) Phase-matching condition. (c) Phase mismatch condition. Figure taken from [18]

To achieve the phase-matching condition given by Eq. (2.15) for a specific fundamental wavelength, one must find at what angle it is satisfied. This situation is illustrated in Fig. 2.4 a). As Fig. 2.4 b) suggests, this occurs when $\bar{k}$ makes an angle θ_m to the optic axis, called the phase-matching angle. For a different angle, destructive interference between the emitted SH waves reduces the conversion efficiency, as shown in Fig. 2.4 c). Experimentally, the phase-matching angle can be found by recording the SH intensity as a function of the angle between the incident beam and the optic axis of the crystal.

Due to the birefringent properties that allow light to experience two different refractive indices, the phase-matching condition (2.15) can be fulfilled, as illustrated by the gray line in Fig. 2.5 a). Hence, in the context of angle tuning, Eq. (2.15) can be rewritten as:

$$n_o(\lambda_1) = n_e(\lambda_2, \theta_m). \tag{2.18}$$

This condition together with Eq. (2.17) leads to:

$$\frac{1}{n_o(\lambda_1)^2} = \frac{\sin^2\theta_m}{\bar{n}_e^2(\lambda_2)} + \frac{\cos^2\theta_m}{n_o^2(\lambda_2)}, \tag{2.19}$$

which can be simplified by replacing $\cos^2\theta_m$ by $1-\sin^2\theta_m$ and solving for $\sin^2\theta_m$

$$\sin^2\theta_m = \frac{\frac{1}{n_o^2(\lambda_1)} - \frac{1}{n_o^2(\lambda_2)}}{\frac{1}{\bar{n}_e^2(\lambda_2)} - \frac{1}{n_o^2(\lambda_2)}} \implies \theta_m = \sin^{-1}\left(\sqrt{\frac{\frac{1}{n_o^2(\lambda_1)} - \frac{1}{n_o^2(\lambda_2)}}{\frac{1}{\bar{n}_e^2(\lambda_2)} - \frac{1}{n_o^2(\lambda_2)}}}\right). \tag{2.20}$$

Equation (2.20) shows how the crystal should be oriented to achieve phase matching, resulting in constructive interference, as seen in Fig. 2.4b). When this condition is not met, destructive interference occurs as SH waves go out of phase; see Fig. 2.4 c). A non-linear optic crystal has a unique range of phase-matching angles within the range $[0, \frac{\pi}{2}]$ corresponding to a specific range of fundamental wavelengths, implied by the Sellmeier coefficients. The physical meaning of θ_m is illustrated in Fig. 2.5 b).

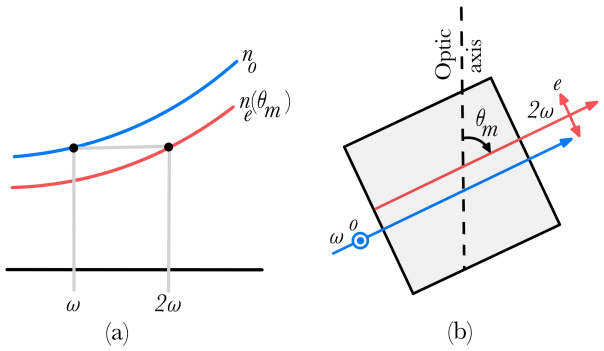

Figure 2.5: (a) Angle tuning involves matching the ordinary refractive index n_o, and the extraordinary refractive index $n_e(\theta_m)$. (b) Fundamental wave incident on a negative uniaxial nonlinear crystal at angle θ to the optic axis such that $n_o(\omega_o) = n_e(2\omega_0, \theta_m)$. Adapted from [11].

2.3.2 Phase-matching bandwidth

Since ultrashort pulses have a broad spectrum, it is impossible to phase match the whole spectrum, as in the monochromatic case. This means that there is a bandwidth for which phase matching is achievable for a certain central wavelength.

As mentioned earlier, the crystal length must be kept within the coherence length in order for efficient SHG to occur. Hence, the interaction process has a phase mismatch tolerance of [11]:

$$|\Delta k| \leq \frac{2}{L}. \tag{2.21}$$

Equation (2.21) implies that small deviations from frequencies that exactly satisfy the phase-matching condition $\Delta k(\omega_1) = 0$ are tolerated insofar as the condition $\omega_1 + \omega_1 = \omega_2$ is satisfied. As a result, the phase-matching bandwidth can be defined as [11]:

$$\Delta\nu = \frac{c_0}{2\pi L}\frac{1}{|N_2 - N_1|}, \tag{2.22}$$

where N_1, N_2 are the group indices of the material at ω_0 and $2\omega_0$ respectively. The group refractive indices can be calculated according to [11]:

$$N_i = n_j(\lambda_c) - \lambda_c \frac{dn_j}{d\lambda}\bigg|_{\lambda=\lambda_i} \; ; \; i = 1, 2, \; j = o, e, \tag{2.23}$$

where $n(\lambda)$ is given by the Sellmeier equations (4.4) and λ_0 is the wavelength of the fundamental that the bandwidth centers around. Equation 2.22 implies that a larger L decreases the phase-matching bandwidth, while a smaller L increases it.

2.4 High harmonic generation

The SH light can be used to produce even higher harmonics via HHG. This process occurs when laser pulses focused on a gas reach intensities of the order of 10^{14} W/cm^2 [13]. This section briefly introduces HHG and the cutoff law that can be used to estimate the maximum photon energy that can be generated via HHG.

2.4.1 The high-harmonic spectrum

As mentioned in the Introduction, the highly non-linear process of HHG is described by a regime completely different from that of SHG. HHG can only be initiated by laser pulses of sufficiently high intensities. The magnitudes of the laser electric field must be in the order of the electric field

of the atomic potential. As a result, the Coulomb potential is greatly distorted, enabling highly non-linear optical processes and the emission of optical overtones of the driving laser field. The resulting harmonic spectrum consists of a comb of odd-order harmonics, equally spaced by twice the driving frequency. [5]

Figure 2.6 presents a schematic representation of an HHG spectrum. For low harmonic orders, shown in blue, the intensity decreases rapidly with increasing harmonic order. This is known as the perturbative region. After a certain energy, all the harmonics have a comparable intensity. This region is known as the plateau. This behavior cannot be explained using a perturbative treatment of P(t) as in Eq. 2.1. Finally, at even higher orders, the intensity drops sharply, defining the so-called harmonic cut-off region.

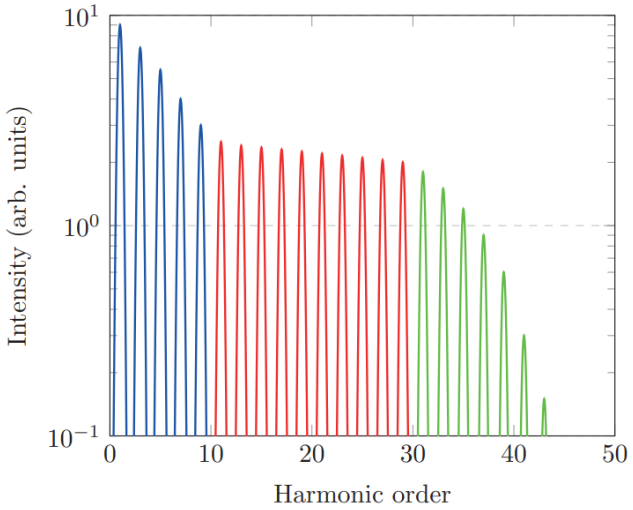

Figure 2.6: Schematic sketch of the relative intensity of harmonics in logarithmic scale. Three distinct regions are indicated by color. Blue peaks represent the perturbative region, red peaks constitute the plateau region, and the highest orders, marked green, make up the cutoff region. Figure taken from [5].

2.4.2 The 3-step model

The so-called 3-step model, used to explain HHG, is based on a semi-classical approach. As the name suggests, it can be decomposed into three steps (see Fig. 2.7). In the first step, an electric field of sufficient strength bends the atom's Coulomb potential, giving rise to a potential barrier through which a valence electron can tunnel. In the second step, the laser field accelerates the electron away from the parent ion, but when there is a change of sign in the electric field, the electron is driven back to the ion. In the third step, the recombination of the electron with the ion leads to the emission of an XUV photon of energy:

$$\hbar\Omega = I_p + E_k, \tag{2.24}$$

where Ω is the angular frequency of the XUV light, I_p is the ionization potential of the neutral atom, and E_k is the electron's kinetic energy at the moment of the recombination. [13]

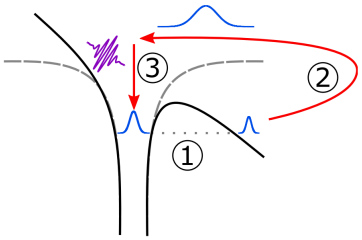

Figure 2.7: The 3-step model in a schematic representation. 1) A laser field perturbs the atomic potential (dashed gray curve), creating a potential barrier (black curve) through which the electron can tunnel. 2) The electron follows a classical trajectory as it propagates in the continuum, accelerating away and being driven back to the ion by the Coulomb field. 3) The electron recombines with the ion, giving rise to the emission of an attosecond XUV pulse. Figure taken from [13].

Neglecting the influence of the ionic potential, the electron's trajectory in a linearly polarized laser field, the maximum kinetic energy is limited to $3.17U_p$, where U_p is the ponderomotive energy, defined by the following universal law:

$$U_p = \frac{E_0^2 e^2}{4 m_e \omega^2} \propto \lambda_c^2 I, \tag{2.25}$$

where ω is the angular frequency of the driving laser, λ_c is the central wavelength, and I is the laser intensity. This explains the origin of the cutoff frequency in Fig. 2.6, which is the frequency at which the non-perturbative region abruptly ends. This frequency corresponds to the cutoff energy given by [7]:

$$E_{\text{cutoff}} = I_p + 3.17U_p, \tag{2.26}$$

where I_p is the ionization energy

Equation (2.25) indicates that generating high-energy photons requires low frequencies and high intensities of the driving laser. Thus, using higher frequency SH radiation to drive HHG means a decrease in U_p, in turn, reduces the cutoff energy E_{cutoff} according to Eq. (2.26).

Although the number of observable harmonics is reduced when using high-frequency fundamental radiation, the single-atom generation efficiency scales with wavelength approximately as $\lambda^{-5.5}$ [7], meaning that the HHG becomes increasingly more efficient for higher-frequency radiation.

Chapter 3

Experimental method

3.1 Experimental setup

This thesis uses a titanium-sapphire laser (Ti:Sa). It has a pulse duration of 25 fs and an energy of 4.8 mJ per pulse. Its central wavelength is 800 nm, and its bandwidth is approximately 70 nm. Short pulses are produced in the Ti:Sa oscillator. The laser system is based on a technique called Chirped Pulse Amplification (CPA), where the pulses undergo stretching and amplification, followed by compression, which generates ultra-short pulses of high intensity. The experimental setup is placed after the compressor (see Fig. 3.1).

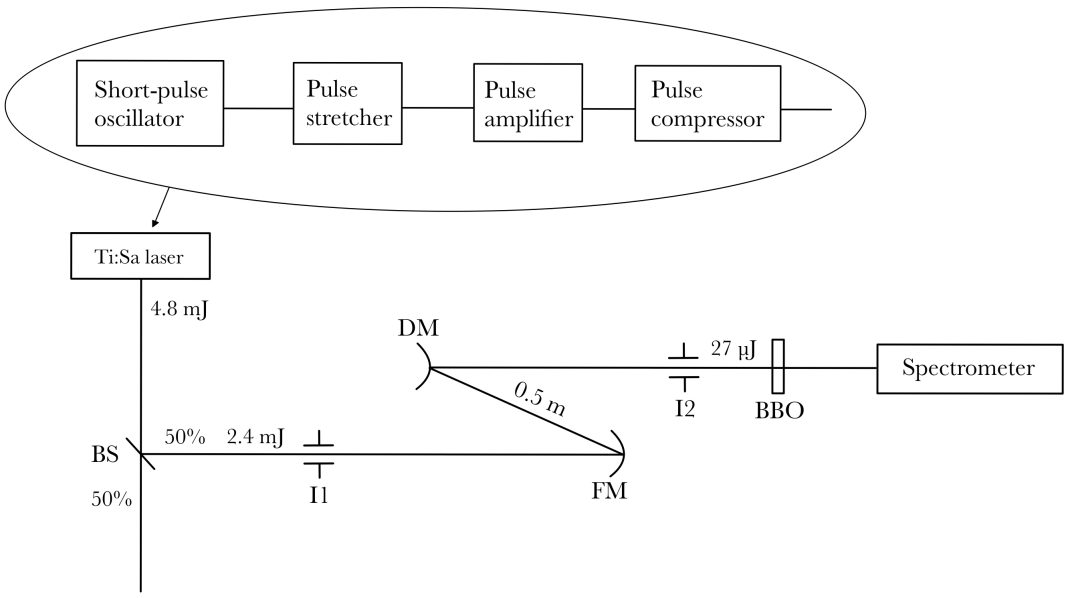

Figure 3.1: Schematic diagram of the experimental setup, which includes the Ti:Sa laser with its components: a beamsplitter (BS) followed by an iris (I1), a focusing mirror (FM), and a diverging mirror (DM) arranged as a telescope, followed by another iris (I2), and the BBO crystal right before the spectrometer. The different pulse energies at the different stages of the setup are also presented. The figure is not to scale.

As illustrated in Fig. (3.1), the generated laser beam enters the beam splitter, splitting it into the reflected arm and the transmitted arm, each carrying half the intensity of the incident. The reflected arm is directed toward the experimental setup, while the transmitted arm is sent to the HHG setup, which was not used for this thesis. The two irises were used to align the setup. The second iris also controlled the energy of the pulses sent to the BBO. No diffraction pattern was observed since the second iris was close to the crystal. The two mirrors are placed in a telescope

arrangement. Usually, for SHG the fundamental beam is focused on the BBO. However, in this case, due to the high energy of the pulses and their short duration, even with loose focusing, the intensity at focus would be too large and would damage the crystal. For this reason, in this project, a telescope is used to reduce the beam size while keeping it collimated. The focusing mirror is concave and has a focal length of 1 m, while the diverging mirror is convex with a focal length of -0.5 m, reducing the beam size by a factor of two, from 13.3 mm to 6.65 mm. The diverging mirror is placed one focal length from the focusing mirror (see Fig. 3.1). This distance ensures that the beams reflected from the diverging mirror are collimated. This implies that the beam radius does not change over the medium length.

Fig. 3.2 a) presents the beam profile measured at the laser output. Fig. 3.2 b) shows how the intensity is spatially distributed in the horizontal direction, while Fig. 3.2 c) shows the spatial intensity distribution in the vertical direction. In both cases, the Gaussian fit is plotted as a reference. Lastly, Fig. 3.2 d) compares the profiles in the two directions, indicating some degree of discrepancy between them. Overall, Fig. 3.2 the beam is not a perfect Gaussian. However, section 5.2 assumes a beam in order to simplify calculations.

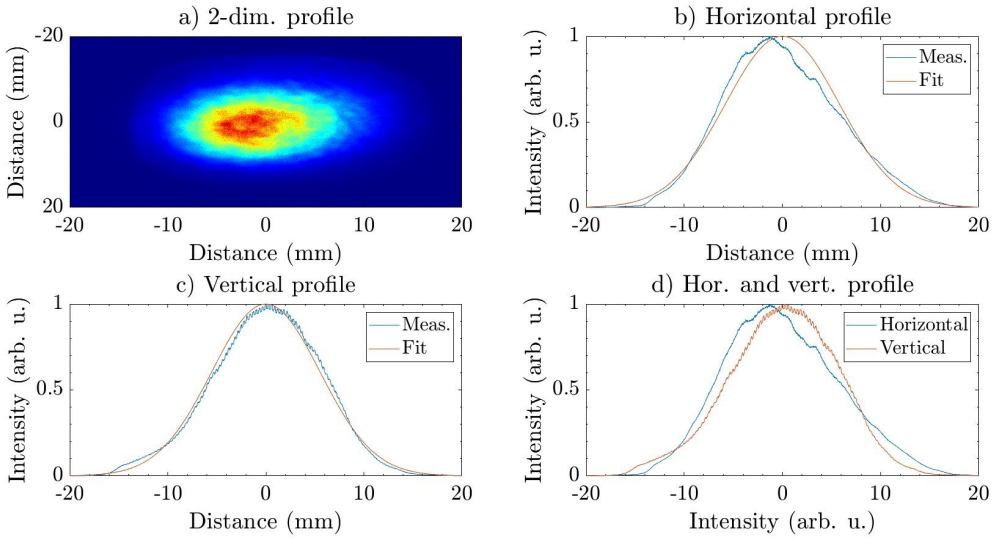

Figure 3.2: Beam profile of Ti:Sa laser. a) 2D spatial intensity distribution of the beam. in 2D. The color indicates the intensity, where red is the highest intensity (arb. u.) and blue is the lowest. b) Measured horizontal profile measured (blue) and Gaussian fit (red). c) Measured vertical profile (blue) and Gaussian fit (red). d) Measured horizontal and vertical profiles plotted simultaneously.

3.2 Angle tuning

The BBO crystal is mounted on a rotation mount attached to a rotation stage. Two BBO crystals are used for the experiments, one with a thickness of $L = 2$ mm and the other of $L = 200$ µm. The rotation stage has scale in arcminutes, where $60' \equiv 1°$. A stage rotation ($\Delta\theta$) corresponds to a change in the incident angle, which is the angle between the incident beam and the axis normal to the surface of the crystal. Each incident angle θ_i is defined as the angle between the normal axis of the crystal and the ray of the incident beam. The optical axis of the BBO is oriented such that when the beam hits the BBO with normal incidence, the k-vector will have an initial phase-matching angle of $\theta_m = 29.2°$.

The reference spectrum was obtained by placing an AvaSpec-3648 spectrometer directly between I2 and the BBO. This spectrometer has a broader wavelength range than the AvaSpec-ULS4096CL-EVO spectrometer of higher resolution, which was used to acquire the SH signal spectra. The

various SHG spectra were measured for incidence angles between $-100'$ and $100'$ in steps of $10'$. This corresponds to a variation of the phase-matching angle from $27.10°$ to $31.53°$.

Chapter 4

Simulations

This section presents the results of the numerical simulations. The simulations are based on the equations and assumptions presented in Chapter 2 and allow studying the spectral properties of the SH intensity for a range of phase-matching angles prior to the experiments.

4.1 Second harmonic intensity (revisited)

Recalling Eq. (2.12), I_2, for a given wavelength λ_1, is also dependent on the angle through the following equation [18]:

$$I_2 = \frac{32\pi^2}{n_e(\theta, \lambda_1/2) n_o(\lambda_1)^2 \lambda_1^2 \epsilon_0 c^3} d_{\text{eff}}^2 I_1 L^2 \,\text{sinc}^2\left(\frac{|\Delta k(\theta)|L}{2}\right), \tag{4.1}$$

where d_{eff} denotes the effective nonlinear coefficient. For the BBO crystals used in this thesis, the value of d_{eff} is given by [19]:

$$d_{\text{eff}} = d_{31} \sin\theta - d_{22} \cos\theta \sin 3\phi, \tag{4.2}$$

under type I phase-matching conditions (for interpretation of d_{31} and d_{22}, see Appendix). The azimuthal angle in the xy plane ϕ for the BBO crystals used in this thesis is 90° [20]. The angle θ defines the incident angle between the propagation vector and the crystalline z axis, which is generally aligned with the optical axis. The d-components included in d_{eff} are listed in the following table.

Table 4.1: Specific values for d_{22} and d_{31} for the BBO crystals used in this thesis. Data taken from [20].

d_{jk}	d_{jk} (C/V^2)
d_{22}	2.0×10^{-23}
$d_{15} = d_{31}$	7.5×10^{-25}

Furthermore, $\Delta k(\theta)$ in Eq. (4.1) is given by:

$$\Delta k(\theta) = \frac{4\pi}{\lambda_1}[n_o(\lambda_1) - n_e(\lambda_2, \theta)], \tag{4.3}$$

where n_o and $n_e(\lambda_2, \theta)$ is given by Eq. (4.4) below and Eq. (2.17), respectively. With the constants for the specific BBO crystal used in this project, the Sellmeier equations (2.16) for the full transparency range ($410 - 3300$ nm) are given by [20]:

$$n_o^2(\lambda) = 2.7366122 + \frac{0.0185720}{\lambda^2 - 0.0178746} - 0.0143756\lambda^2 \tag{4.4}$$

$$\bar{n}_e^2(\lambda) = 2.3698703 + \frac{0.0128445}{\lambda^2 - 0.0153064} - 0.0029129\lambda^2, \tag{4.5}$$

where λ is given in µm.

4.2 Results

4.2.1 Second-harmonic efficiency as a function of wavelength and angle

Figure 4.1 presents the SH efficiency as a function of the fundamental wavelength 740 nm $< \lambda_1 <$ 860 nm and the phase-matching angle $27.10° < \theta_m < 31.53°$ (range obtained from Eq. (2.20)) for a flat input spectrum (i.e., $I_1(\lambda) = 1$) for $L = 2$ mm and $L = 200$ µm.

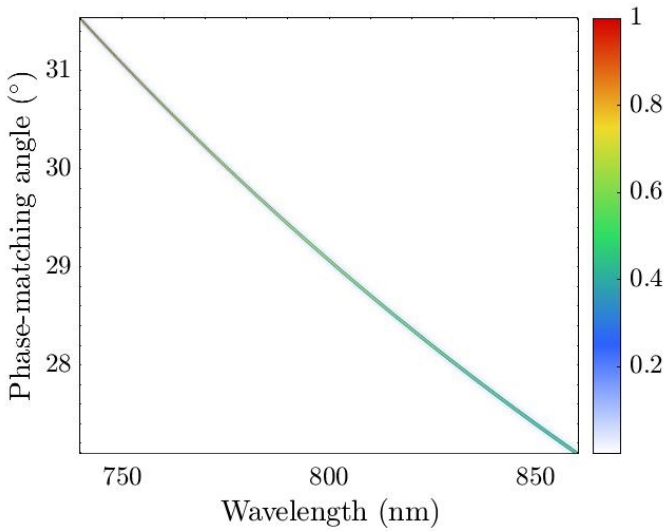

(a) $L = 2$ mm

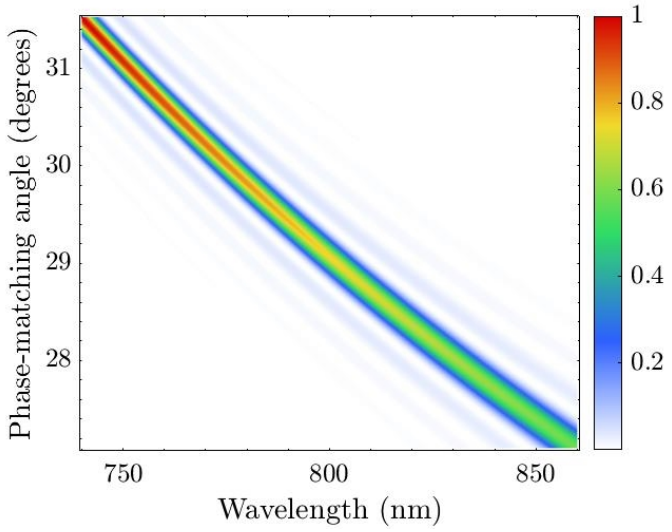

(b) $L = 200$ µm

Figure 4.1: Normalized SH conversion efficiency (indicated by the color scale) based on a flat spectrum as a function of wavelength and phase-matching angle for two different BBO crystal thicknesses.

Figure 4.1 shows that the phase-matching angle strongly depends on the fundamental wavelength. In particular, the figure further shows that an increase in wavelength is associated with a decrease in phase-matching angle within the plotted range. The wavelength dependence of the phase-matching angle allows tuning of the SH signal. The efficiency is optimal along this curve because $|\Delta k|$ is minimized along the curve, as shown in Fig. 4.2.

Fig. 4.1 also shows an optimal efficiency region, reaching a maximum for a fundamental wavelength of 740 nm and a phase-matchng angle around 31.53°. This can be explained by the λ^{-2} scaling in Eq. (4.1). Furthermore, by taking the absolute value of Eq. (4.3), $|\Delta k|$ reaches its minimum value of $3.24 \cdot 10^{-9}$ m^{-1} for these specific wavelength and phase-matching angle values, further explaining why the maximum efficiency occurs at this point.

A comparison of Fig. 4.1b) and Fig. 4.1a) shows that in the thinner crystal (200 µm), for a given phase-matching angle, the range of wavelengths that are efficiently phase-matched is broader than for the thicker crystal (2 mm). This is linked to the fact that the phase-matching bandwidth is inversely proportional to the length of the medium, as shown in Eq. (2.22).

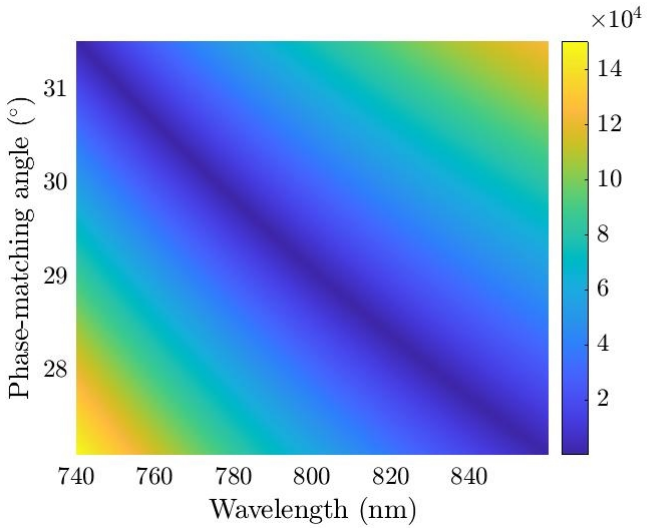

Figure 4.2: Magnitude of the phase mismatch Δk [m^{-1}] as a function of fundamental wavelength and phase-matching angle.

In reality, the spectrum of the fundamental laser pulses is not flat. Fig. 4.3 shows the spectrum of the Ti:Sa laser used in this project.

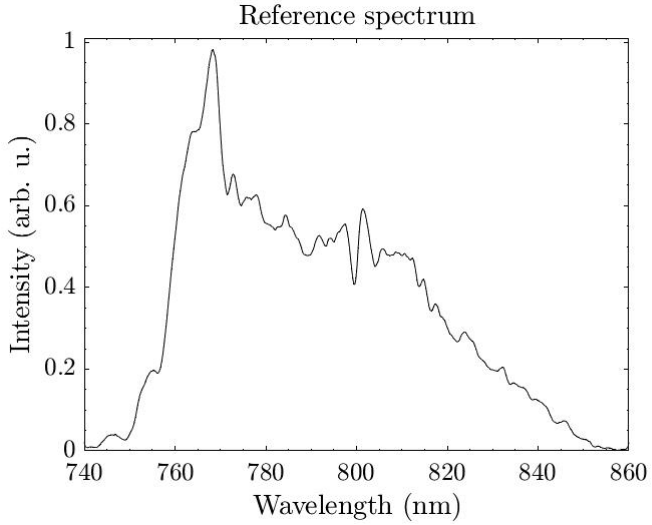

Figure 4.3: Reference spectrum (normalized) collected from Avantes software, interpolated with 500 points to improve the resolution.

The spectrum ranges from 740 nm to 860 nm and shows how the spectral intensity of the IR pulses

varies for the different wavelengths, peaking at 768.62 nm. Using this spectrum, Fig. 2.13 shows the conversion efficiency as a function of the fundamental wavelength and the phase-matching angle for the different crystal thicknesses.

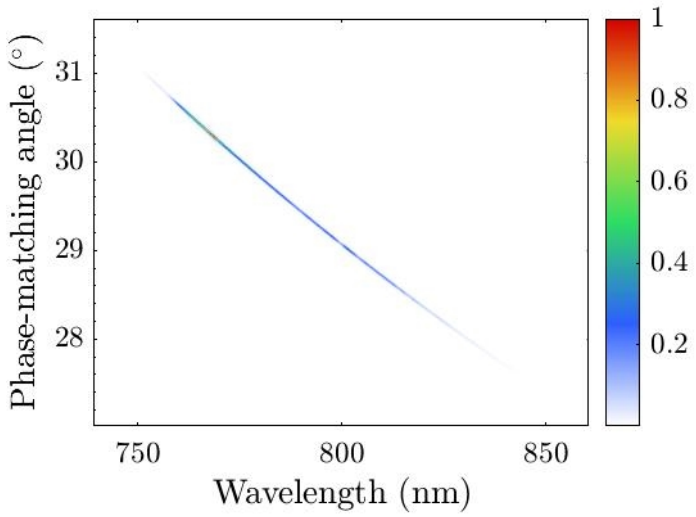

(a) $L = 2$ mm

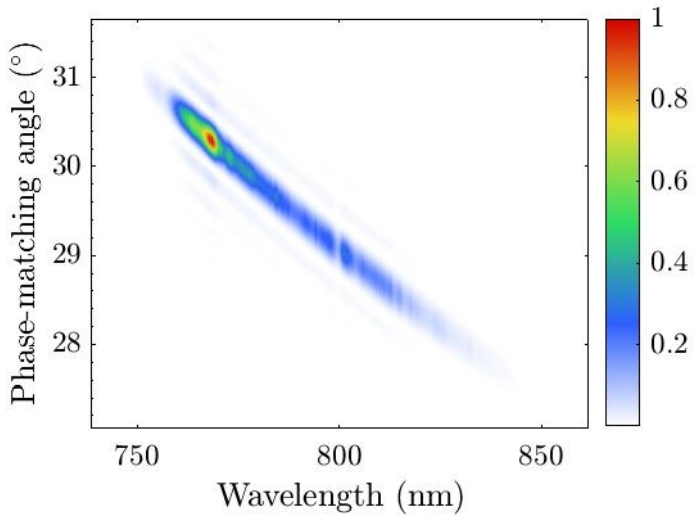

(b) $L = 200$ µm

Figure 4.4: Normalized SH conversion efficiency (indicated by the color scale) based on the reference spectrum above as a function of wavelength and phase-matching angle for two different BBO crystal thicknesses.

As Fig. 4.4 shows, there is a modulation in the efficiency map due to the reference spectrum in Fig. 4.3. This feature is particularly prominent in Fig. 4.4b. To verify that this modulation is not caused by numerical errors, the same calculations were performed using a smooth input spectrum, which obtained a smooth efficiency map.

For both crystals of lengths ($L = 2$ mm and $L = 200$ µm), shown in Fig. 4.4, the maximum conversion efficiency corresponds to a fundamental wavelength of 768.62 nm, which is the wavelength corresponding to the maximum input intensity in Fig. 4.3. This can be explained by the intensity dependence of Eq. (4.1). Moreover, the phase mismatch corresponding to this maximum efficiency is $\Delta k = -15.58$ m^{-1}, which may seem large at first. However, the argument of the sinc function

$\frac{|\Delta k|L}{2} = 0.02$, which is still relatively low. However, Fig. 4.2 shows that the magnitude of the wave vector mismatch rapidly reaches values of the order of 10^4, therefore minimizing Δk is crucial since the argument of the sinc function can quickly increase due to a small change in Δk.

Compared to the case of a flat spectrum, the efficiencies in Fig. 4.4 are smaller. This is explained by the fact that the efficiency (Eq. 2.13), depends on the intensity of the input. In particular, at a wavelength of 740 nm and a minimum magnitude of the mismatch wave vector, Fig. 4.4 shows almost zero conversion efficiency. This is due to the fact that at 740 nm, the input intensity is negligible, as seen in Fig. 4.3. However, the efficiency map in Fig. 4.4 follows as in Fig. 4.2, suggesting that keeping $|\Delta k|$ low or within reasonable values is critical for optimizing the efficiency, with the thinner crystal giving rise to a broader phase-matching bandwidth.

4.2.2 Second-harmonic spectra

For each experimental SH spectrum obtained, a theoretical spectrum is plotted for comparison. In order to generate theoretical simulations for each angle tested experimentally, the refraction of the incident laser beam must be considered [18].

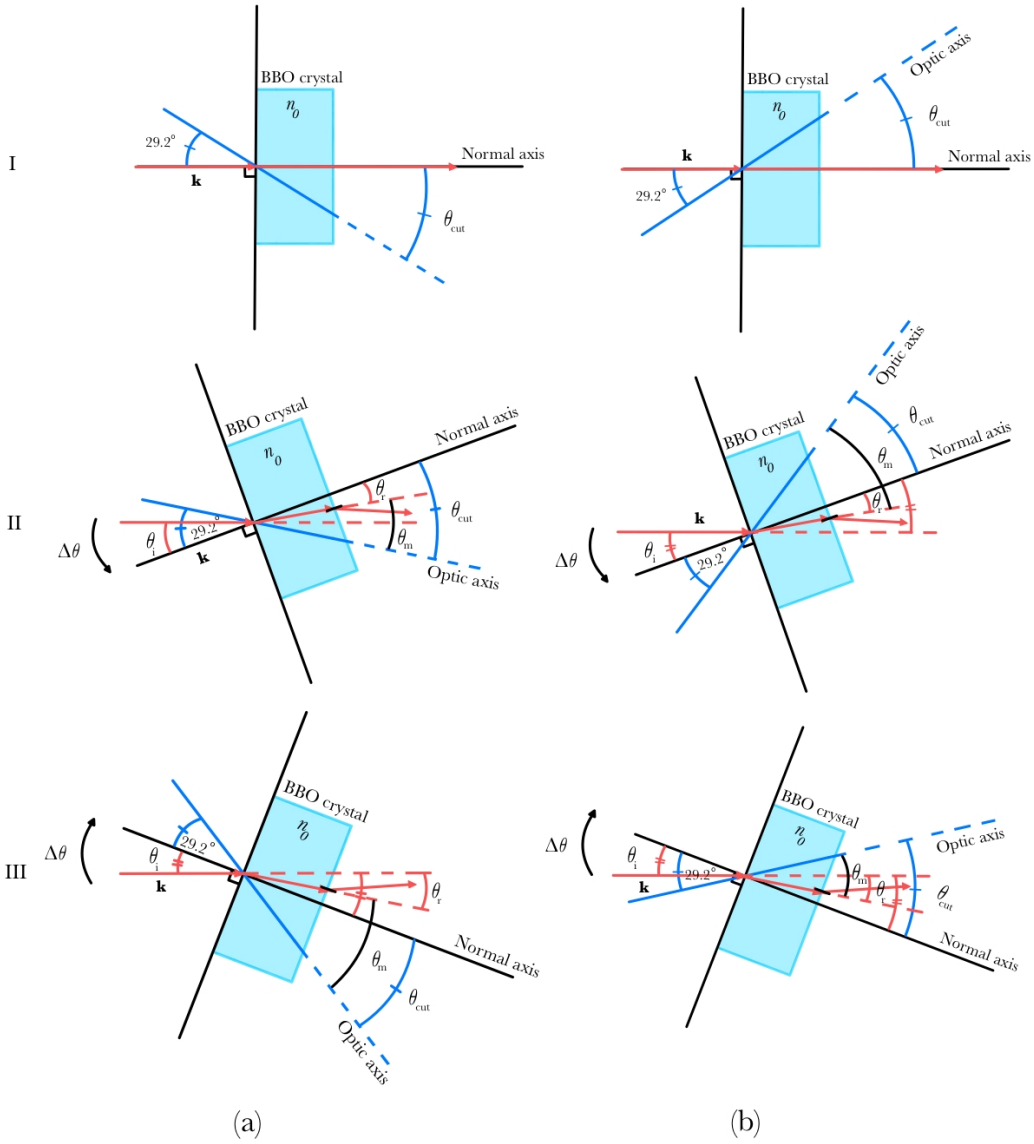

Figure 4.5: Schematic representation of refraction effects modifying the path of the incident laser beam through the nonlinear crystal due to a stage rotation. a) The beam path for the thin BBO with $L = 200$ µm. b) The beam path for the thick BBO with $L = 2$ mm. I: initial position of the BBO crystal, II: positive angular displacement and the subsequent beam path, and III: the effects on the beam path of a positive angular displacement. Note that the ordinary refractive index, n_o, is indicated as only the fundamental beam is considered. Figure not to scale.

In Fig. 4.5, the incident angle θ_i is given by the magnitude of the angular displacement $\Delta\theta$ from the experiment. The BBO is cut with an angle of $\theta_\mathrm{cut} = 29.2°$ [20] defining the angle between the normal and the optic axis. The refractive index of the ordinary beam is as usual denoted by n_o[2]. Angles θ_r and θ_m denote the angle of refraction and the phase-matching angle, respectively. A clockwise angular rotation corresponds to a positive angular displacement ($\Delta\theta > 0$), and an anticlockwise rotation corresponds to a negative angular displacement ($\Delta\theta < 0$) in the rotation stage. Depending on the sign of $\Delta\theta$, this leads to an increase or a decrease in θ_m. From Fig. 4.5,

[2]Here, n_o is given by the Sellmeier equation from (4.4) where $\lambda = \lambda_\mathrm{c}$, λ_c being the central wavelength obtained from Eq. (4.9) based on the reference spectrum in Fig. 4.3.

θ_m can be calculated from the geometry and Snell's law, which is given by [18]:

$$n_{\text{air}} \sin\theta_{\text{i}} = n_o(\lambda_{\text{c}}) \sin\theta_{\text{r}} \overset{n_{\text{air}}=1}{\Longrightarrow} \theta_{\text{r}} = \arcsin\left(\frac{\sin\theta_{\text{i}}}{n_o(\lambda_{\text{c}})}\right). \tag{4.6}$$

In the different cases in Fig. 4.5, the phase-matching angle is given by:

$$\theta_m = \begin{cases} \theta_{\text{i}} + \theta_{\text{cut}} & \text{a) III, b) II in Fig.4.5} \\ \theta_{\text{cut}} - \theta_{\text{r}} & \text{a) II, b) III in Fig.4.5} \end{cases}. \tag{4.7}$$

Moreover, the actual thickness is slightly longer than the crystal thickness for a non-zero angular displacement.

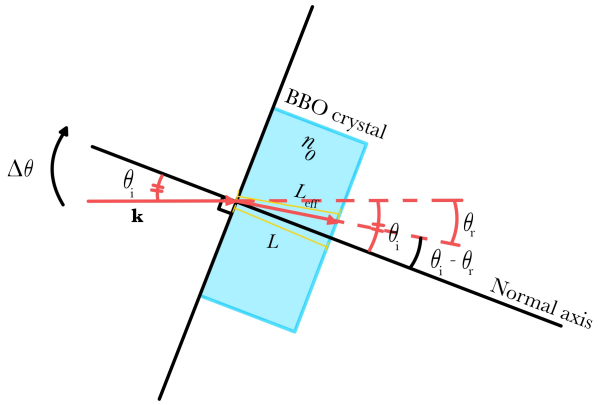

Figure 4.6: Geometry for determining the effective thickness of the BBO crystal. Not to scale.

Given the geometry in the Fig. 4.6, the effective crystal thickness is given by:

$$L_{\text{eff}} = \frac{L}{\cos(\theta_i - \theta_r)}. \tag{4.8}$$

Lastly, to calculate n_o, the central wavelength is needed. For a given SH spectrum, it can be calculated in the following way [18]:

$$\lambda_{\text{c}} = \frac{\int \lambda I(\lambda) d\lambda)}{\int I(\lambda) d\lambda}, \tag{4.9}$$

where

$$I(\lambda) = \begin{cases} 0 & \text{if } I(\lambda) < 0.5\text{max}\{I(\lambda)\}, \\ I(\lambda) & \text{if } I(\lambda) \geq 0.5\text{max}\{I(\lambda)\} \end{cases}. \tag{4.10}$$

Chapter 5

Experimental results and discussion

In this chapter, the experimentally obtained SH spectra for various incident angles are presented and analyzed. Theoretical comparisons are also made. The HHG cutoff energies for a chosen incident angle were also calculated for the two crystals used in the experiments.

5.1 Second harmonic spectra

In total, 42 spectra were obtained, one spectrum for each incident angle for a given crystal length. Figure 5.1 presents the measured SH spectra in red for four different incident angles. The figure shows that as the incident angle changes from $-50'$ to $-80'$, the central wavelength of the SH radiation changes from 394 to 391 nm. The experimental results are compared with the numerical simulations presented in blue. The numerical simulations qualitatively reproduce the experimental results. However, there are a few notable differences between the experiments and the theory, which are discussed below.

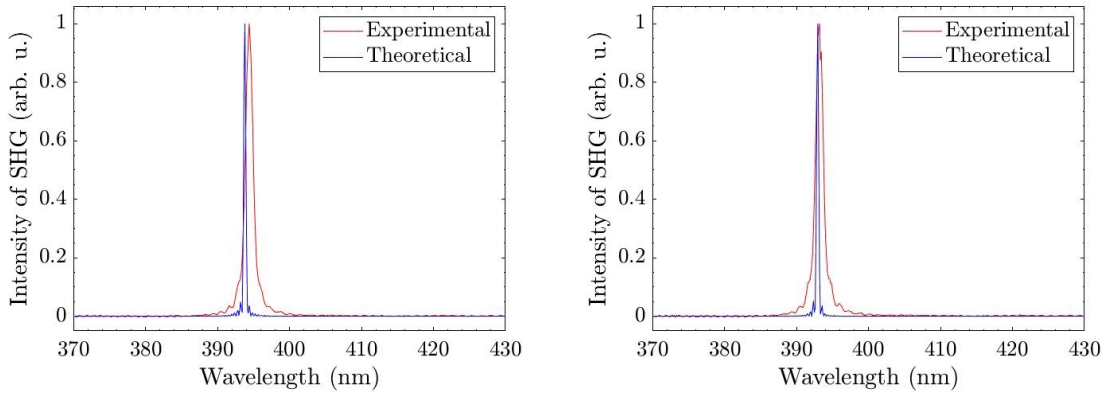

(a) $\theta_{\mathrm{i}} = -50'$ (b) $\theta_{\mathrm{i}} = -60'$

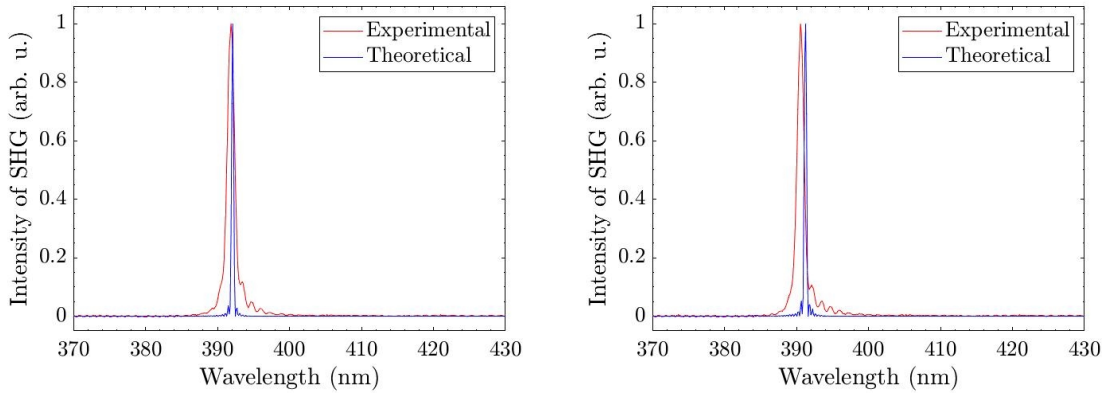

(c) $\theta_{\mathrm{i}} = -70'$ (d) $\theta_{\mathrm{i}} = -80'$

Figure 5.1: Selected experimental and corresponding theoretical normalized second-harmonic spectra for different angles of incidence for $L = 2$ mm. The theoretical spectra are obtained from (4.1) with a fixed phase-matching angle, calculated from the incident angle according to Eq. (4.7).

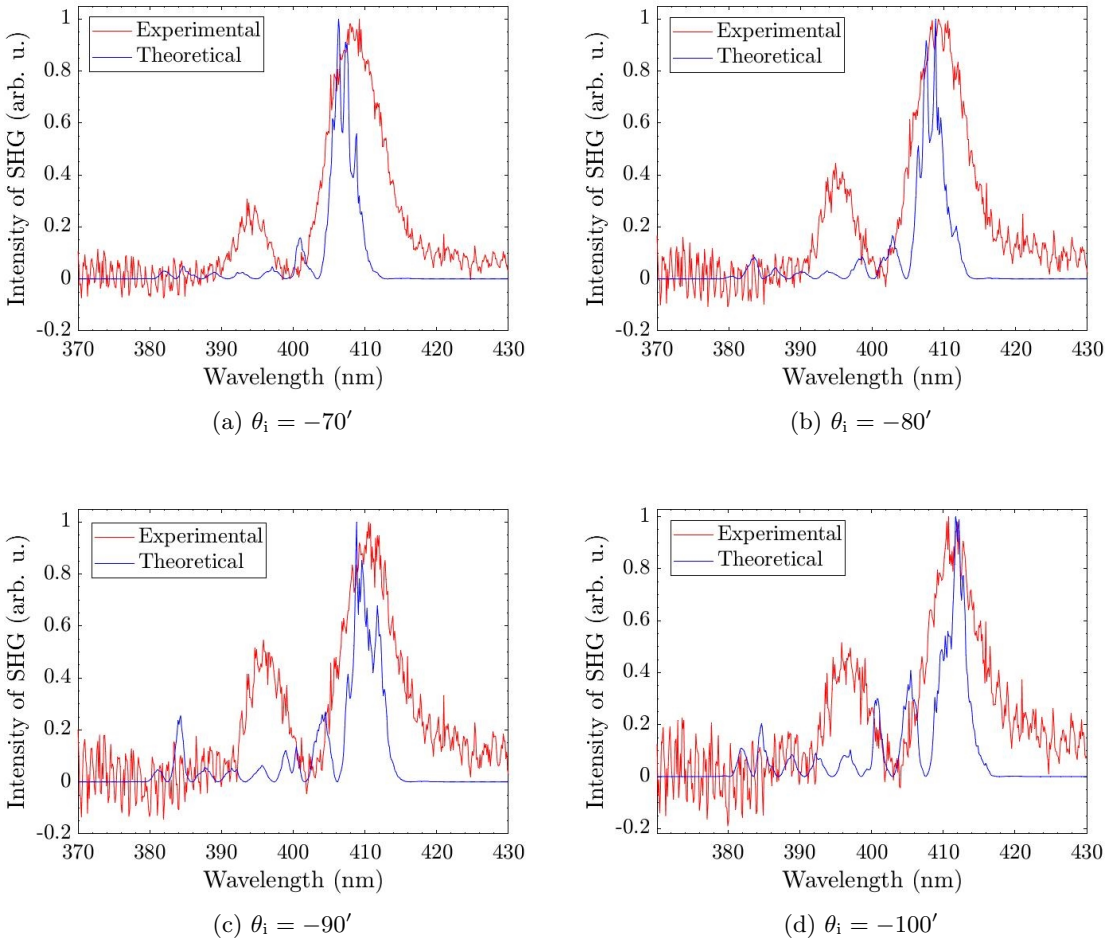

(a) $\theta_i = -70'$ (b) $\theta_i = -80'$

(c) $\theta_i = -90'$ (d) $\theta_i = -100'$

Figure 5.2: Selected experimental and corresponding theoretical normalized second-harmonic spectra for different angles of incidence for $L = 200$ µm. Theoretical spectra are obtained from Eq. (4.1) with a fixed phase-matching angle, calculated from the incident angle according to Eq. (4.7).

Figure 5.2 presents similar plots to those shown in Fig. 5.1 but in the case of the thin crystal (200 µm). The figure shows that as the incident angle changes from $-70'$ to $-100'$, the central wavelength of the SH radiation changes from 409 to 412 nm. In contrast to the 2 mm crystal, the experimental and theoretical spectra are broader. Experimentally, the spectra are also more noisy, especially for large negative input angles (see Fig. 5.2 a) and Fig. 5.2 d)).

Fig. 5.2 also suggests that a crystal length of $L = 200$ µm gives rise to broader SH spectra compared to $L = 2$ mm, shown in Fig. 5.2. This can be explained by the inverse L-dependence of the phase-matching bandwidth in Eq. (2.22) and is further supported by the simulations. Because of the shorter interaction length, the thinner crystal is more tolerant to phase mismatch according to Eq. (2.21), giving rise to a spectrally broader SH signal over a wider range of wavelengths and angles [8]. A longer interaction length requires precise phase matching, where even a small phase mismatch can cause destructive interference by Eq. (2.21), significantly reducing the width of the SH signal [11].

As seen in both Fig. 5.1 and 5.2, the experimental and theoretical spectra have similar characteristics but are not identical. The key features are similar: the experimental spectra demonstrate the expected behavior of sinc^2 in Eq. (4.1). However, the experimental SH peak is slightly shifted in comparison to the theoretically predicted peaks for both crystal lengths. Another difference between the experimental and simulated signal spectra is that the period of an oscillation of the

experimental is larger than that of the theoretical, as seen in Figs. 5.1 and 5.2.

The deviation of the experimental central wavelengths from the theoretically predicted ones can be caused by several factors. First, the spectral resolution was limited, resulting in the loss of finer spectral features. Hence, this could give rise to a broader experimental spectrum. Second, the spectrometer may not have been calibrated accurately, leading to a shift in the central wavelength.

Figures 5.1 and 5.2 only present a small subset of all the measurements. In. Fig. 5.3, the phase-matching angle is plotted as a function of the central wavelength of the SH signal for the 2 mm crystal (a) and for the 200 µm (b).

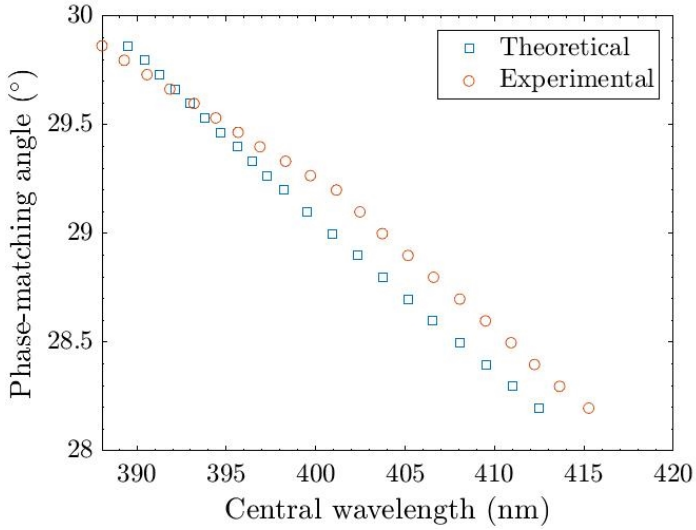

(a) $L = 2$ mm

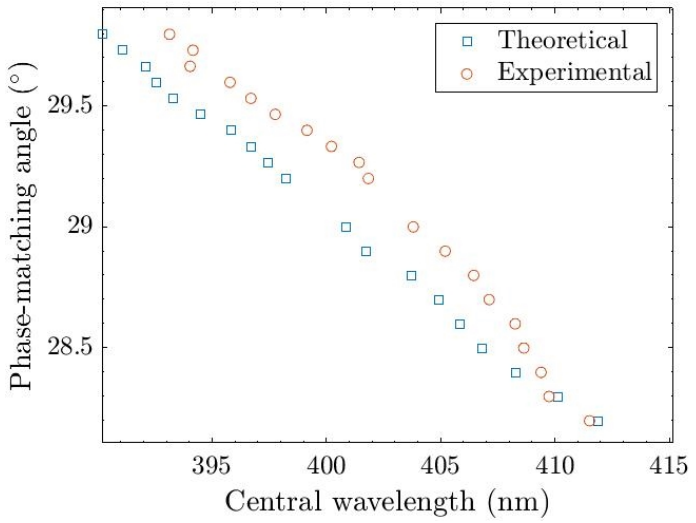

(b) $L = 200$ µm

Figure 5.3: Experimental and corresponding theoretical plot of the tested phase-matching angles θ_m, against central wavelength λ_c for the two BBO crystals. For b), the points $\theta_i = -10', 100'$ corresponding to $\theta_m = 28.69°, 28.01°$ are removed due to an error in the measurements.

As seen in Fig. 5.3, an increase in the fundamental wavelength leads to a decrease in the phase-matching angle. The relationship between θ_m and λ_c can be verified by the relationship in the

simulations; see Fig. 4.4, where an increase in the fundamental wavelength leads to a decrease in θ_m.

Figure 5.3 further shows that, due to the broad bandwidth of the fundamental laser pulse, the central wavelength of the emitted SH radiation depends on the angle of the BBO crystal with respect to the incident laser beam as in Eq. (2.20) suggests.

The differences between the experimental and theoretically calculated central wavelengths range from 0.06% to 0.74% for $L = 2$ mm and $0.09 - 6.70\%$ for $L = 200$ µm. The differences between the phase matching angles corresponding to the theoretically predicted central wavelengths and those corresponding to the experimental central wavelengths fall within $0.05 - 0.79\%$ for $L = 2$ mm and $0.08 - 6.21\%$ for $L = 200$ µm. These indicate relatively small discrepancies. Hence, they are likely to be caused by the factors discussed above.

5.2 Estimation of the cut-off energy

This section discusses the possibility of driving HHG with the generated SH pulses and estimates the cut-off energy that would be reached for both crystals. The SH spectra of the incident angle $\theta_\mathrm{i} = 0'$ for both crystal lengths are used for the calculations.

In the following, it is assumed that the SH radiation generated is sent to the HHG setup and focused in an argon gas cell to generate high-order harmonics. First, the pulse energy must be calculated. Because the SH radiation is not separated from the fundamental, the reference spectrum, measured before the BBO, and the SH spectrum, measured after the BBO, were used instead of measuring the power before and after the BBO. The spectra in the frequency domain for $L = 2$ mm are shown below.

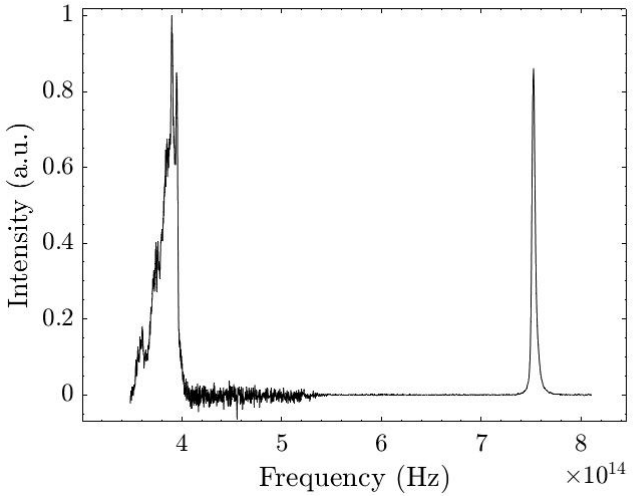

Figure 5.4: Normalized and calibrated spectrum of fundamental and SH radiation in the frequency domain for $\theta_\mathrm{i} = 0°$ i.e., $\theta_m = 29.2°$.

As a measure of the area under the curve of the reference spectrum and the SH spectrum in Fig. 5.4, the following quantities are introduced:

$$S_\omega = \int_{\nu_\mathrm{start}}^{\nu_\mathrm{end}} s(\nu) d\nu, \tag{5.1}$$

$$S_{2\omega} = \int_{\nu_\mathrm{start}/2}^{\nu_\mathrm{end}/2} s(\nu) d\nu. \tag{5.2}$$

From S_ω and $S_{2\omega}$, the peak energies of the fundamental and the SH radiation, respectively, are given by:

$$E_\omega = \frac{P_{\text{ave}}}{R_r} \tag{5.3}$$

$$E_{2\omega} = \frac{S_{2\omega}}{S_\omega} E_\omega, \tag{5.4}$$

where P_{ave} is the average power of the beam, which is 0.08 W, measured before the beam enters the crystal, and R_r is the repetition rate, which is 3 kHz. The pulse energy of the SH signal for each crystal is:

$$E_{2\omega} = 3.02 \cdot 10^{-6} \text{ J for } L = 2 \text{ mm, and} \tag{5.5}$$

$$E_{2\omega} = 5.04 \cdot 10^{-7} \text{ J for } L = 200 \text{ µm.} \tag{5.6}$$

The results indicate that for the 2 mm crystal, the SH pulses have an energy of almost an order of magnitude higher than for the 200 µm crystal. This is explained by the longer interaction length, which leads to a higher SH intensity in the thicker crystal. In addition, the much higher pulse energy for the 2 mm crystal indicates that the SHG is more efficient for the thicker crystal.

Next, the pulse duration of the SH signal for each BBO must be calculated. The pulse duration given by Eq. (2.14), in which $\Delta\nu$ is estimated from the full-width half maximum (FWHM) in the frequency domain:

$$\Delta\tau = \frac{\gamma}{\Delta\nu}, \tag{5.7}$$

where $\gamma = 0.44$ for Gaussian beams. The resulting pulse durations are:

$$\tau = 118 \text{ fs for } L = 2 \text{ mm, and} \tag{5.8}$$

$$\tau = 25 \text{ fs for } L = 200 \text{ µm.} \tag{5.9}$$

This shows that the 200 µm crystal generated shorter pulses than the 2 mm crystal, which is due to the larger phase-matching bandwidth.

The beam waist radius after the lens is given by [11]:

$$w = \frac{\lambda_c f}{\pi w_0}, \tag{5.10}$$

where f is the lens's focal length, which is 0.5 m, and w_0 is the beam waist radius before the lens, which is assumed to be 13.3 mm, which is a common beam size.

The intensity at the beam's focus can be found in two different ways [11], [7]:

$$I_{\text{focus}} = \frac{2E_{2\omega}}{\Delta\tau A};\ A = \pi w^2, \tag{5.11}$$

$$I_{\text{focus}} = \frac{c\epsilon_0}{2}|E_0|^2. \tag{5.12}$$

Using Eq. (5.11),

$$I_{\text{focus}} = 7.21 \cdot 10^{13} \text{ W/cm}^2 \text{ for } L = 2 \text{ mm, and} \tag{5.13}$$

$$I_{\text{focus}} = 5.65 \cdot 10^{13} \text{ W/cm}^2 \text{ for } L = 200 \text{ µm.} \tag{5.14}$$

These values are similar. In the case of 2mm BBO, the energy is higher while the pulse duration is longer, and for 200 µm, the pulse energy is lower while the pulse duration is shorter, leading to similar values of the intensity at focus. Moreover, at 800 nm, the HHG intensity is usually of the order of 10^{14} W/cm^2 [13], indicating that the intensities are on the edge of being able to generate higher harmonics. The use of SH signals is expected to have lower energy as a result of

an imperfect SHG conversion efficiency.

Finally, Eq. (2.25), can be written as:

$$U_p = \frac{E_0^2 e^2 \lambda_c^2}{4 m_e \pi^2 c^2}, \tag{5.15}$$

where λ_c is the central wavelength of the SH signal. From Eq. (5.15), the cutoff energy is estimated from Eq. (2.26), where $I_p = 15.76$ eV [21]. The values of E_{cutoff} along with the calculated quantities above are summarized in Table 5.1.

Table 5.1: Values of SH energy $E_{2\omega}$, pulse duration $\Delta\tau$, intensity at focus I_{focus}, ponderomotive energy U_p, and cutoff energy E_{cutoff} for $L = 2$ mm and $L = 200$ µm.

L	$E_{2\omega}$ (J)	$\Delta\tau$ (fs)	I_{focus} (W/cm^2)	U_p (eV)	E_{cutoff} (eV)
2 mm	$3.03 \cdot 10^{-6}$	118	$7.21 \cdot 10^{13}$	4.28	20.04
200 µm	$5.04 \cdot 10^{-7}$	25	$5.65 \cdot 10^{13}$	3.37	19.13

As seen in Table 5.1, both crystals result in similar values of E_{cutoff}. The reason for this is that the longer crystal generates SH waves of higher energy but with a longer pulse duration, while the shorter crystal generates SH radiation of lower energy but with a shorter pulse duration, see Eq. (5.11). On the basis of these results, it is clear that the BBO thickness has to be optimized to find the best compromise between the energy and pulse duration of the emitted SH. Furthermore, the values of U_p in Table 5.1 are relatively small, indicating that it might be possible to generate low-order harmonics. There are two factors for the relatively small values of U_p; one is that the SH intensity at focus is low, and the other is that the wavelength of the driving radiation is lower for SH radiation, see Eq. 2.25.

Chapter 6

Conclusions and outlook

6.1 Conclusions

This thesis investigated the generation and optimization of SHG for application to HHG. This was done by sending a Gaussian laser beam through anisotropic crystals. Two BBO crystals of different thicknesses ($L = 2$ mm and $L = 200$ µm) were used, and the results were compared. The crystals were rotated by various angles in order to phase-match different parts of the incident beam's spectrum, and the obtained SH signal spectra were compared with simulations.

One of the biggest challenges when optimizing SHG with the Ti:Sa laser pulses is that the beam incident on the crystal must be kept large. Focusing the beam in the crystal must be avoided because the beam size would be too small, which would burn the crystal due to a short pulse at high energy. For this reason, the beam is instead collimated in order to reach sufficiently high intensities to obtain the SHG. The telescope reduces the beam size while keeping the beam collimated.
The results show that due to the broad bandwidth of the fundamental laser, the central wavelength of the emitted SH radiation is highly dependent on the phase-matching angle, which, in turn, is related to the incident angle of the laser. In this way, using ultra-short laser pulses to drive the SHG allows tuning of the SH signal by rotating the crystal with respect to the incident beam.

A key difference between the two crystals is that the thicker crystal produces a narrower bandwidth of the SH spectra compared to that of the thinner crystal. In exchange, SH signals get more energy due to the longer interaction length, making SHG more efficient. The fact that the thinner crystal can support broadband phase matching is due to the inverse relationship between the crystal length and the phase-matching bandwidth. Thus, depending on the purpose, either can be utilized to optimize SHG. If higher SH efficiencies are required at the expense of precise phase matching, a thicker BBO may be useful. When a broader coverage wavelength in the SH signal is required at the expense of reduced conversion efficiency, the thinner BBO may be more suitable.

The experimental results compared to the simulations are in good agreement. The experimental results reproduce key features of experiments, where the thickness affects the phase-matching bandwidth, and by changing the angle, one can tune the central wavelength of SHG. The exact central wavelength for a given angle does not match perfectly with the simulations, primarily due to the spectrometer's limited resolution and imperfect calibration.

The estimated cut-off energies showed that, in principle, reasonable intensities for HHG can be reached. However, the cut-off energies are lower than what could be expected at 800 nm, meaning that the intensities of the generated SH signal are on the edge of being able to generate higher-order harmonics. Hence, an HHG spectrum would show very low orders of higher harmonics. Nevertheless, this is expected by the square relationship between the ponderomotive energy and the central wavelength of the driving laser.

6.2 Outlook

The next step is to implement and optimize the setup in a scheme for optimal HHG efficiency. In this way, SHG can be used as fundamental radiation to drive HHG. Consequently, the SHG must be optimized for that particular purpose. This involves finding a compromise between the crystal thickness and the pulse duration. In this project, the intensity was kept low in order not to burn the crystal. However, in principle, the intensity could have been increased to get more energy out. Lastly, since the calculated SH intensities at focus are low for HHG, one could use a lens of a focal length shorter than 50 cm to reach higher intensities in the HHG gas cell.

In this project, SHG was optimized independently of HHG to study the different factors that influence SH signals. A range of potential developments in the setup include the use of filters of various types. Firstly, placing a filter between the BBO and the spectrometer allows one to study the phase-matching angles producing the highest SH intensity peaks for specific colors instead of optimizing directly according to a reference spectrum, which is highly fluctuating. Secondly, a short-pass filter can be used to block the fundamental beam emerging from the BBO and reduce the signal-to-noise ratio, which would be particularly suitable for thinner crystals with lower output SH intensities. On the same note, since the thick BBO generated better intensities of the SH signals but with narrower phase-matching bandwidths, a non-collinear geometry could be implemented in a way that allows its bandwidth to increase [8]. Lastly, a wider range of angles could be investigated experimentally.

Chapter 7

Appendix

7.1 Derivation of the coupled-amplitude equations for the monochromatic infinite plane-wave case

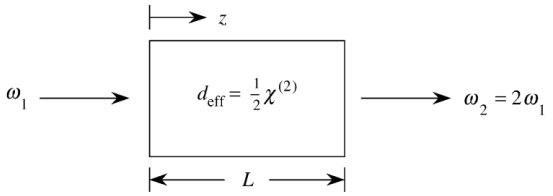

Figure 7.1: Collinear second-harmonic generation in a nonlinear crystal. The fundamental frequency is ω_1, and ω_2 denotes the frequency of the SH wave. Moreover, z is the propagation direction of the collinear waves, d_{eff} is the effective d-value, and L is the crystal length. Figure from [9]

Consider the case of collinear beams in Fig. 7.1 and an electric field that is a superposition of two monochromatic plane waves of frequencies ω_1 and $\omega_2 = 2\omega_1$ of slowly varying amplitudes $A_1(z)$ and $A_2(z)$, propagating in the z-direction in a non-linear crystal. The electric field strength is given by [8]:

$$E(z,t) = \sum_{j}^{2} \text{Re}\{A_j(z)e^{i(\omega_j t - k_j z)}\} = \sum_{j=\pm1,\pm2} \frac{1}{2} A_j e^{i(\omega_j t - k_j z)}, \tag{7.1}$$

where $\omega_{-j} = -\omega_j$ and $A_{-j} = A_j^*$. The induced polarization giving rise to SHG is given by:

$$P^{\text{NL}}(z,t) \overset{(2.1)}{=} \epsilon_0 \chi^{(2)} E(z,t)^2 \overset{(7.1)}{=} 2d_{\text{eff}}\epsilon_0 \cdot \frac{1}{4} \sum_{j,q=\pm1,\pm2} A_j A_q e^{i((\omega_j+\omega_q)t-(k_j+k_q)z)}. \tag{7.2}$$

Substituting Eq. (7.1) and Eq. (7.2) in Eq. (2.6) leads to a single differential equation (DE), of many terms, each corresponding to a harmonic function of a distinct frequency. By matching terms at each of the frequencies ω_1 and ω_2 on both sides of the DE, it can be separated into two time-independent DEs. The two DEs can be written as two one-dimensional Helmholtz equations with associated sources [11]:

$$(\nabla^2 + k_1^2)A_1 e^{-ik_1 z} = -4\frac{1}{c^2\epsilon_0} d_{\text{eff}} \omega_1^2 A_2 A_1^* e^{i(k_2-k_1)z} \tag{7.3}$$

$$(\nabla^2 + k_2^2)A_2 e^{ik_2 z} = -2\frac{1}{c^2\epsilon_0} d_{\text{eff}} \omega_2^2 A_1^2 e^{2ik_1 z}. \tag{7.4}$$

Since the fields only depend on the longitudinal coordinate z, ∇^2 can be replaced by $\frac{d^2}{dz^2}$. Hence, Eq. (**??**) becomes:

$$\begin{aligned}&\left[\frac{d^2A_1}{dz^2} - 2ik_1\frac{dA_1}{dz} - k_1^2A_1 + k_1^2A_1\right]e^{ik_1z} + \text{c.c.}\\&= \frac{-2d_{\text{eff}}\omega_1^2}{c^2\epsilon_0}A_2A_1^*e^{i(k_2-k_1)z} + \text{c.c.}.\end{aligned} \tag{7.5}$$

We can drop complex conjugate terms from each side and still maintain equality, which results in the following:

$$\frac{d^2A_1}{dz^2} + 2ik_1\frac{dA_1}{dz} = \frac{-4d_{\text{eff}}\omega_1^2}{c^2}A_2A_1^*e^{-i(2k_1-k_2)z}. \tag{7.6}$$

Often, the first term on the left-hand side is neglected on the grounds that it is much smaller than the second term. This is the approximation known as the slowly varying amplitude approximation (SVEA) or the envelope approximation and is valid whenever [9]:

$$\left|\frac{d^2A_1}{dz^2}\right| << \left|k_1\frac{dA_1}{dz}\right|. \tag{7.7}$$

This requires that the fractional change in A_1 in a distance of the order of an optical wavelength must be much smaller than 1. When this approximation is made, we have the following:

$$\frac{dA_1}{dz} = \frac{2id_{\text{eff}}\omega_1^2}{k_1c^2}A_2A_1^*e^{-i\Delta kz} \tag{7.8}$$

Analogous arguments for the components A_2 and P_2 hold for the generated SH wave at 2ω that is governed by Eq. (7.4). Hence, the coupled-wave equations take the following form:

$$\frac{dA_1}{dz} = \frac{2i\omega_1^2d_{\text{eff}}}{k_1c^2}A_2A_1^*e^{-i\Delta kz} \tag{7.9}$$

$$\frac{dA_2}{dz} = \frac{i\omega_2^2d_{\text{eff}}}{k_2c^2}A_1^2e^{i\Delta kz}, \tag{7.10}$$

where

$$\Delta k = 2k_1 - k_2 \tag{7.11}$$

7.2 Solution for the case $\Delta k \neq 0$

Given that $\Delta k \neq 0$, Eq. (7.10) can be integrated directly, leading to:

$$A_2(L) = i\frac{4\omega_1^2}{k_2c^2}d_{\text{eff}}A_1^2\int_0^L e^{i\Delta kz}dz = i\left(\frac{4\omega_1^2}{k_2c^2}\right)d_{\text{eff}}A_1^2\frac{e^{i\Delta kL}-1}{i\Delta k}. \tag{7.12}$$

The intensity is directly proportional to the square of the amplitude according to [9]:

$$I_i = 2n_i\epsilon_0c|A_i|^2, i = 1, 2. \tag{7.13}$$

By taking the absolute value of Eq. (2.11) and using the fact that

$$\left|\frac{e^{i\Delta kL}-1}{i\Delta k}\right| = (\ldots) = L^2\frac{\sin^2\left(\frac{\Delta kL}{2}\right)}{\left(\frac{\Delta kL}{2}\right)^2} \equiv L^2\,\text{sinc}^2\left(\frac{\Delta kL}{2}\right), \tag{7.14}$$

the intensity of the SH field I_2, in terms of the intensity of the incident field I_1 is given by:

$$\begin{aligned}I_2(L) &= \frac{32n_2\epsilon_0\omega_1^4}{k_2^2c^3}d_{\text{eff}}^2\left(\frac{I_1(0)^2}{4n_1^2\epsilon_0c^2}\right)L^2\,\text{sinc}^2\left(\frac{\Delta kL}{2}\right) = \frac{8\omega_1^2d_{\text{eff}}I_1^2}{n_2n_1^2\epsilon_0c^3}L^2\,\text{sinc}^2\left(\frac{\Delta kL}{2}\right)\\&\overset{\omega_1=\frac{2\pi}{\lambda_1}}{=}\frac{32\pi^2}{n_2n_1^2\lambda_1^2\epsilon_0c^3}d_{\text{eff}}^2I_1^2L^2\,\text{sinc}^2\left(\frac{\Delta kL}{2}\right).\end{aligned} \tag{7.15}$$

where Eq. (2.8) is used in the second equality.

7.3 The effective d-value

The components of the second-order susceptibility tensor $\chi^{(2)}(\omega_2, \omega_1, \omega_1)$ (where $\omega_2 = 2\omega_1$) for SHG are defined as the proportionality constants that relate the amplitude of the non-linear polarization density to the product of the electric field amplitudes by:

$$P_i^{\mathrm{NL}}(\omega_2) = \epsilon_0 \sum_{jk} \chi_{ijk}^{(2)}(\omega_2, \omega_1, \omega_1) E_j(\omega_1) E_k(\omega_1) = 2\epsilon_0 \sum_{jk} d_{ijk} E_j(\omega_1) E_k(\omega_1), \;\; i, j, k = 1, 2, 3 \tag{7.16}$$

where $P_i(\omega_2), E_j(\omega_1)$, and $E_k(\omega_2)$ are the components of these vectors along the crystal's principal axes. The Cartesian components of the fields are given by the indices ijk. In the last equality, $d_{ijk}(2\omega; \omega, \omega) = \frac{1}{2}\chi_{ijk}^{(2)}(\omega, \omega)$ is used [11]. For a fixed geometry (i.e., fixed propagation polarization directions), it is possible to express the polarization density vector $\mathbf{P}(\omega_2)$ from (7.16) as a scalar relationship:

$$P(\omega_2) = 2\epsilon_0 d_{\mathrm{eff}} E(\omega)^2; \;\; P(\omega) = |\mathbf{P}(\omega)| \text{ and } E(\omega) = |\mathbf{E}(\omega)|, \tag{7.17}$$

where $d_{\mathrm{eff}} = \frac{1}{2}\chi^{(2)}$ is known as the effective d-value. On matrix form Eq. (7.16) becomes Eq. [11]:

$$\begin{pmatrix} P_x(2\omega) \\ P_y(2\omega) \\ P_z(2\omega) \end{pmatrix} = 2\epsilon_0 \begin{pmatrix} d_{11} & d_{12} & d_{13} & d_{14} & d_{15} & d_{16} \\ d_{21} & d_{22} & d_{23} & d_{24} & d_{25} & d_{26} \\ d_{31} & d_{32} & d_{33} & d_{34} & d_{35} & d_{36} \end{pmatrix} \begin{pmatrix} E_x(\omega)^2 \\ E_y(\omega)^2 \\ E_z(\omega)^2 \\ 2E_y(\omega)E_z(\omega) \\ 2E_x(\omega)E_z(\omega) \\ 2E_x(\omega)E_y(\omega) \end{pmatrix} \tag{7.18}$$

Bibliography

[1] P. A. Franken, A. E. Hill, C. W. Peters, and G. Weinreich, "Generation of optical harmonics," *Phys. Rev. Lett.*, vol. 7, pp. 118–119, Aug. 1961.

[2] A. Zheltikov, A. LHuillier, and F. Krausz, *Nonlinear Optics*, pp. 161–251. Berlin, Heidelberg: Springer Berlin Heidelberg, 2012.

[3] A. McPherson, G. Gibson, H. Jara, U. Johann, T. S. Luk, I. A. McIntyre, K. Boyer, and C. K. Rhodes, "Studies of multiphoton production of vacuum-ultraviolet radiation in the rare gases," *J. Opt. Soc. Am. B*, vol. 4, p. 595, 1987.

[4] M. Ferray, A. L'Huillier, X. Li, L. Lompre, G. Mainfray, and C. Manus, "Multiple harmonic conversion of 1064 nm radiation in rare gases," *J. Phys. B*, vol. 21, p. L31, 1988.

[5] H. Laurell, *Attosecond photoelectron interferometry: from wavepackets to density matrices.* Doctoral thesis (compilation), 2023.

[6] H. Laurell, D. Finkelstein-Shapiro, C. Dittel, C. Guo, R. Demjaha, M. Ammitzböll, R. Weissenbilder, L. Neoričić, S. Luo, M. Gisselbrecht, C. L. Arnold, A. Buchleitner, T. Pullerits, A. L'Huillier, and D. Busto, "Continuous-variable quantum state tomography of photoelectrons," *Physical Review Research*, vol. **4**, no. 3, p. 033220, (2022).

[7] R. Weissenbilder, *Optimization of High-order Harmonic Generation for Attosecond Science.* Doctoral thesis (compilation), 2023. Defence details Date: 2023-10-27 Time: 09:15 Place: Lecture Hall Rydbergsalen, Department of Physics, Professorsgatan 1, Faculty of Engineering LTH, Lund University, Lund. External reviewer(s) Name: Hernández-García, Carlos Title: Dr. Affiliation: University of Salamanca, Spain. —.

[8] I. Sytcevich, *Generation, characterization and application of infrared few-cycle light pulses.* PhD thesis, Lund University, Lund, Sweden, 2022.

[9] R. W. Boyd, "Chapter 2 - wave-equation description of nonlinear optical interactions," in *Nonlinear Optics (Third Edition)* (R. W. Boyd, ed.), pp. 69–133, Burlington: Academic Press, third edition ed., 2008.

[10] C. Guo, *A High Repetition Rate Attosecond Light Source Based on Optical Parametric Amplification.* Doctoral thesis (compilation), Faculty of Engineering, LTH, 2018. Defence details Date: 2018-02-09 Time: 13:15 Place: Lecture hall Rydbergsalen, Fysicum, Professorsgatan 1, Lund University, Faculty of Engineering. External reviewer(s) Name: Legare, Francois Title: Professor Affiliation: INRS, Varennes, Canada —.

[11] B. E. A. Saleh and M. C. Teich, *Fundamentals of Photonics, 2 Volume Set.* Wiley, 3rd ed., 2023.

[12] M. Bertocchi, *First principles Second-Harmonic Generation in quantum confined silicon-based systems.* PhD thesis, Ecole Polytechnique X, 2013.

[13] D. Busto, *Quantum interference effects in attosecond photoionization dynamics.* Doctoral thesis (compilation), 2020.

[14] V. Kumar, N. Coluccelli, and D. Polli, "Chapter 5 - coherent optical spectroscopy/microscopy and applications," in *Molecular and Laser Spectroscopy* (V. Gupta, ed.), pp. 87–115, Elsevier, 2018.

[15] D. L. Mills, *Nonlinear Optics: Basic Concepts*. Berlin, Heidelberg: Springer-Verlag Berlin Heidelberg, 2 ed., 1998. Springer Book Archive.

[16] O. Svelto, *Principles of Lasers*. Springer New York, NY, 5 ed., 2010.

[17] K. T. K. K. M. Sasaki, T. Hayashi and T. Kominato, "Transmittance and phase matching of bbo crystal in the 3−5 μm range and its application for the characterization of mid-infrared laser pulses," *Optical Materials Express*, vol. 8, no. 6, pp. 1410–1419, 2018.

[18] W. Dwi Astuti, H. Matsukuma, M. Nakao, K. Li, Y. Shimizu, and W. Gao, "An optical frequency domain angle measurement method based on second harmonic generation," *Sensors*, vol. 21, no. 2, 2021.

[19] R. S. Klein, G. E. Kugel, A. Maillard, A. Sifi, and K. Polgár, "Absolute non-linear optical coefficients measurements of bbo single crystal and determination of angular acceptance by second harmonic generation," *Optical Materials*, vol. 22, no. 2, pp. 163–169, 2003. Proceedings of the Scientific Committe of the French Research Group "GDR 1148 CNRS": LASMAT: Research Group on Laser Materials.

[20] EKSMA Optics, "Beta barium borate (bbo) crystals." https://eksmaoptics.com/nonlinear-and-laser-crystals/nonlinear-crystals/beta-barium-borate-bbo-crystals/. Accessed: 2024-06-22.

[21] National Institute of Standards and Technology (NIST), "NIST Chemistry WebBook: Argon (Ar)." https://webbook.nist.gov/cgi/inchi?ID=C7440371Mask=20, 2024. Accessed: 2024-08-28.